

## Numerical simulations of generic train in crosswind using AVL Fire

*Master's thesis in Complex Adaptive Systems*

PER RINGQVIST

Department of Applied Mechanics  
Division of Fluid Mechanics  
CHALMERS UNIVERSITY OF TECHNOLOGY  
Göteborg, Sweden 2011  
Master's thesis 2011:01



MASTER'S THESIS IN COMPLEX ADAPTIVE SYSTEMS

Numerical simulations of generic train in crosswind using AVL Fire

PER RINGQVIST

Department of Applied Mechanics  
*Division of Fluid Mechanics*  
CHALMERS UNIVERSITY OF TECHNOLOGY  
Göteborg, Sweden 2011

Numerical simulations of generic train in crosswind using AVL Fire

PER RINGQVIST

© PER RINGQVIST, 2011

Master's thesis in Complex Adaptive Systems 2011:01

ISSN 1652-8557

Department of Applied Mechanics

Division of Fluid Mechanics

Chalmers University of Technology

SE-412 96 Göteborg

Sweden

Telephone: +46 (0)31-772 1000

Cover:

LES of train in unsteady cross wind. Isosurface of the Q-invariant  $= 4 * 10^5$ , visualizing resolved instantaneous turbulent structures. Body surface colored with instantaneous pressure. Plane under body colored by instantaneous velocity.

Chalmers Reproservice

Göteborg, Sweden 2011



Master's thesis in Complex Adaptive Systems  
PER RINGQVIST  
Department of Applied Mechanics  
Division of Fluid Mechanics  
Chalmers University of Technology

## ABSTRACT

Many modern trains today have distributed engines in every wagon throughout the train making the leading wagon relatively light. This can cause a risk of derailment, when traveling at high speeds and exposed to strong crosswind or sudden gusts of wind. To study the forces acting on a train as a result of side wind, low Reynolds number experiments on a simplified train geometry has been conducted at the RTRI institute in Japan. The experiments include both stationary yaw angles as well as a train moving through a region of crosswind. The experimental data consists of pressure measurements at 38 locations distributed along the train body.

The simulated scenarios consist of a stationary train exposed to side wind of 5 m/s at yaw angle 90 degrees ( $Re = 16000$ ), as well as a train moving at 5 m/s perpendicular through the side wind ( $Re = 23000$ ). To simulate the moving train a moving velocity profile is used to as a model for the side wind. PANS and LES are run on identical meshes for both cases. The standard Smagorinsky model is employed in the LES. For the RANS part of PANS the  $\zeta$ - $f$ -model is used. The parameter  $f_k$  defined as the unresolved to total ratio of turbulence kinetic energy, is recomputed before each timestep. The mesh for the stationary case is slightly coarser for LES, which makes it possible to see the advantage of PANS. All simulations are performed using the commercial software package AVL Fire.

Good agreement with the experimental data is found with both LES and PANS for the stationary case. However, PANS makes a substantially better prediction of the pressure at the lateral ends of the train, where the spanwise mesh-resolution is coarser. In the moving case LES and PANS displays very similar results, having some discrepancies but showing fair agreement to experimental data. The computing of  $f_k$  assumes a stable time averaged flow, which is the probable reason why PANS does not show the same advantage in the moving scenario.

Keywords: PANS, LES, train, crosswind

## ACKNOWLEDGEMENTS

This project was supported by AVL Fire. I want to thank AVL Fire for the free licenses and their professional support: special thanks to Dr. Branislav Basara, Jurgen Schneider and Albert Van der Meer. I want to thank my supervisor Professor Sinisa Krajnovic for all his help and support. Thanks all you guys at the department who have helped me greatly: Jan Östh, Ragnar Larusson, Andreas Martinsson, Fredrik Ekeröth, Eystenn Helgason, David Uystepuust and Xinke Mu. I am grateful to the RTRI-institute for providing the experimental data, especially to Mr. Koji Nakade who has helped me greatly. I want to acknowledge the Center for Scientific and Technical Computing (C3SE). Thank you Sofia Arvidsson for all your love and support.



# Contents

<b>Abstract</b>	<b>i</b>
<b>Acknowledgements</b>	<b>i</b>
<b>Contents</b>	<b>iii</b>
<b>1 Introduction</b>	<b>1</b>
1.1 Background . . . . .	1
1.2 Previous work . . . . .	1
1.2.1 Experimental scenario . . . . .	2
1.3 Purpose . . . . .	5
1.4 Limitations . . . . .	5
<b>2 Theory</b>	<b>6</b>
2.1 Solving the incompressible Navier-Stokes equations . . . . .	6
2.2 Averaged Navier-Stokes equations . . . . .	7
2.3 PANS . . . . .	8
2.4 LES . . . . .	10
2.5 Measuring mesh resolution at the wall . . . . .	10
2.6 Aerodynamic Coefficients . . . . .	11
<b>3 Method</b>	<b>12</b>
3.1 Computational domains and meshes . . . . .	12
3.2 Boundary conditions modelling a stationary train in crosswind . . . . .	13
3.3 Boundary conditions modelling a moving train in crosswind . . . . .	14
3.4 Numerical setup . . . . .	16
3.4.1 Numerical schemes and parameters . . . . .	16
3.4.2 Initialization and averaging . . . . .	17
<b>4 Results</b>	<b>18</b>
4.1 Stationary Scenario: yaw angle $90^\circ$ . . . . .	18
4.1.1 Instantaneous flow structures . . . . .	18
4.1.2 CFL and $y^+$ . . . . .	19
4.1.3 Validation with experimental pressure data . . . . .	20
4.1.4 Force coefficients . . . . .	22
4.1.5 Resolved and Unresolved Turbulence Kinetic Energy . . . . .	23
4.1.6 Averaged flow field visualization . . . . .	24
4.2 Moving Scenario: train speed 5 m/s . . . . .	26
4.2.1 Visualization of the flow scenario . . . . .	26
4.2.2 Validation with experimental pressure data . . . . .	28
4.2.3 Force coefficients . . . . .	31
4.2.4 Computation of $f_k$ for transient boundary conditions . . . . .	33
<b>5 Discussion and Future Work</b>	<b>35</b>



# 1 Introduction

## 1.1 Background

Crosswind stability has been a research area for decades, since higher speeds and lighter trains largely increases the risk of derailment. Freight trains are both heavier and slower than passenger trains, but when running with empty containers there is a risk of derailment related to crosswind. While the safety aspects of crosswind stability is the most important, is also relevant for passenger comfort, as well as for reducing the fatigue on the train and rail. When talking about a moving train in crosswind, it is convenient to define the yaw angle as the angle between the train direction and the effective crosswind. The effective crosswind is the resulting wind velocity from the negative train motion and the actual crosswind, see figure 1.1.1. The flow around

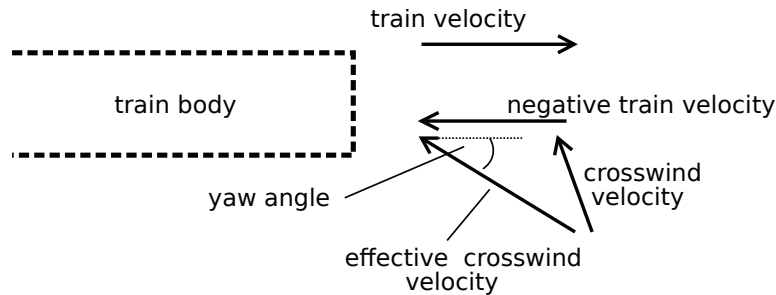


Figure 1.1.1: *The yaw angle is the angle between the train direction and the effective crosswind*

aerodynamic bodies, like a train exposed to crosswind, is highly turbulent. Reynolds Averaged Navier Stokes (RANS) models is a computationally cheap method of computing turbulent flows, but it is computing only the time average of the flow. This is not sufficient since the flow around a train in crosswind is highly time dependent, even in the case of stationary yaw angle. In the case of a train passing through a crosswind gust, this is a transient scenario which does not have a well defined time average. It is possible to solve the Navier Stokes equations (NS) directly, obtaining the time history of the flow. However, due to the chaotic behavior of the solution of NS the computational demands are unrealistic. Large Eddy Simulations (LES), is a method that also resolves the time history of the flow, but is computing a local space average of the flow, hence decreasing the computational demands. LES was performed on an simplified car geometry by Krajnović and Davidson in [8] and [9]. Comparison with experimental data showed that LES is far superior to RANS for this type of aerodynamic flow. However, LES demands very fine resolution of the computational grid (mesh), which limits it to computations at relatively low Reynolds numbers (Re). A full scale train traveling at high speed gives rise to a very large Re, and hence it would be desirable to find a method that could resolve the important transient dynamics but still be feasible for high Re flows. Also for low Re flows we would like a method more robust than LES in regards to insufficient mesh resolution. A promising approach is Partially Averaged Navier Stokes (PANS), recently proposed by Girimaji [5]. PANS offers a way to directly regulate the amount of time averaging in the governing equations. PANS is however less established than LES, and ongoing research is evaluating its capabilities.

## 1.2 Previous work

Crosswind originates from weather conditions which are in general difficult to model. A common experimental setup for crosswind testing is to use a uniform flow generated from a wind tunnel, displacing the aerodynamic body to obtain the desired yaw angle. It is however difficult to do an experiment on a full scale train, simply because it requires an extremely large wind tunnel. Hemida and Krajnovic simulated a high speed train using LES at a steady yaw angle of  $30^\circ$  in [7]. Fairly good agreement with the experimental data was obtained even though the Re in the simulation was seven times lower than in the experiment. However, a steady flow scenario does not reproduce the aerodynamic forces acting on the train when hit by a sudden wind gust [1]. The flow dynamics of a train exposed to a uniform crosswind is not the same as a train passing through a crosswind region of finite propagation in space. Krajnovic, Georgii and Hemida [10] modelled a high speed train exiting a tunnel and passing through a region of varying crosswind. The crosswind was modelled by

prescribing a moving velocity profile on the boundaries on either side of the domain. The shape of the velocity profile was taken from a wind tunnel experiment specifically designed to generate wind gusts of finite length. The underlying flow mechanisms could then be analysed in a scenario that before was considered complex and difficult to simulate. However, the numerical method used was DES (Detached Eddy Simulation), which switches to unsteady RANS-modelling near the walls in order to save computational resources. This means that important details of the flow could potentially be missed, and there was no experimental data available to evaluate the accuracy of the simulations. The wind gust model is shown in figure 1.2.1, comparing it to the model used in this thesis.

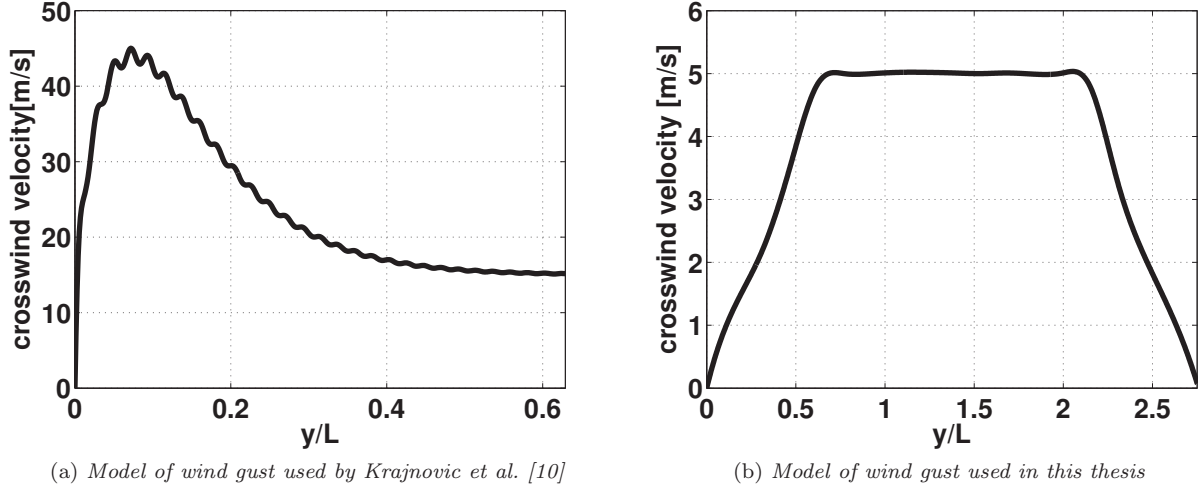


Figure 1.2.1: Comparison of models for wind gusts. The distance on the x-axis is normalized by the current train length  $L$ .

Noting the difference in length of the profiles compared to the train, it can be mentioned that Krajnovic et al. used two locomotives with a wagon in the middle, while the geometry in this thesis is a generic train model having the length of only one wagon. The differences in crosswind speed is also due to the fact that this thesis deals with a low Re scenario. In the experimental work providing data for this thesis, the same wind tunnel was used for testing the stationary yaw angles as for the train passing through a crosswind region. The crosswind generated by the wind tunnel is hence not specifically designed to resemble that of a wind gust occurring in nature. However, the experimental data is still invaluable when evaluating whether our computer models are capable of recreating this type of transient scenarios.

### 1.2.1 Experimental scenario

In the experiments, the side wind is generated by a wind tunnel nozzle, blowing in perpendicular direction to the train motion. The crosswind speed in the wind tunnel nozzle is 5 m/s at all times. Several train velocities are tested: 1, 2, 3, 4 and 5 m/s. The corresponding yaw angles is also tested on a stationary train;  $90^\circ$ ,  $79^\circ$ ,  $68^\circ$ ,  $59^\circ$ ,  $51^\circ$ , and  $45^\circ$ . Note however that the effective crosswind speed in the moving cases does not correspond to 5 m/s. For example when the train is moving with 5 m/s, the effective crosswind is  $\sqrt{5^2 + 5^2} \approx 7$  m/s. In this thesis simulations are done only for the stationary case  $90^\circ$  and the moving case with train velocity 5 m/s. A schematic view of the experimental setup is presented below in figure 1.2.2, together with the reference coordinate system.

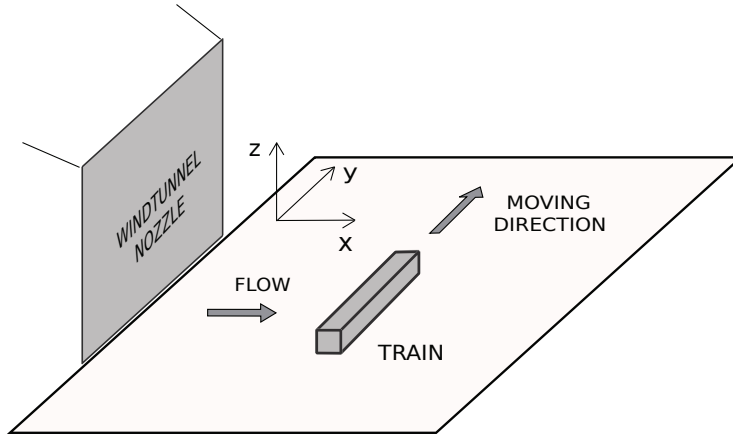


Figure 1.2.2: Schematic view of the experimental setup and reference coordinate system.

The train speed is supposed to be constant during the passage past the wind tunnel nozzle, see figure 1.2.3

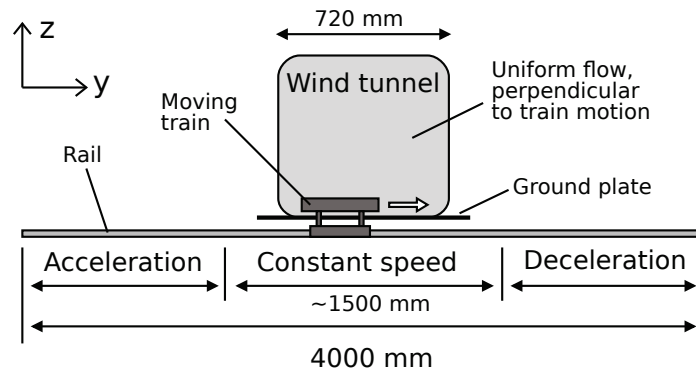


Figure 1.2.3: The train accelerates, reaches constant speed, and decelerates after passing the wind tunnel nozzle.

The pressure is measured at 38 locations distributed along three cross-sections along the train, as well as the front and rear of the body. Below figure 1.2.4 shows the train geometry and the measurement points; note that the train geometry is basically a cuboid mounted on two support cylinders. Figure 1.2.5 shows the dimensions of the train body. The cylinders continue down through a slit in the ground board, where they connect to

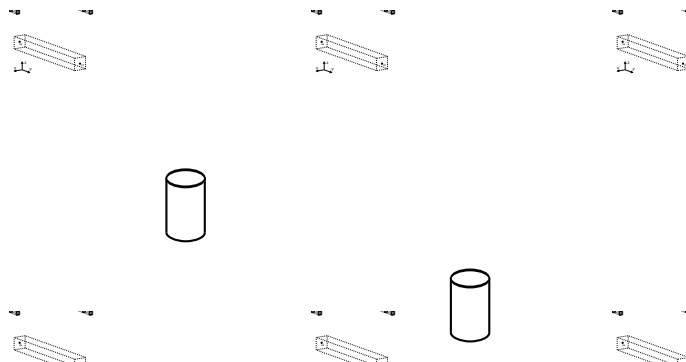


Figure 1.2.4: The points on the train body where the pressure is measured during the experiment.

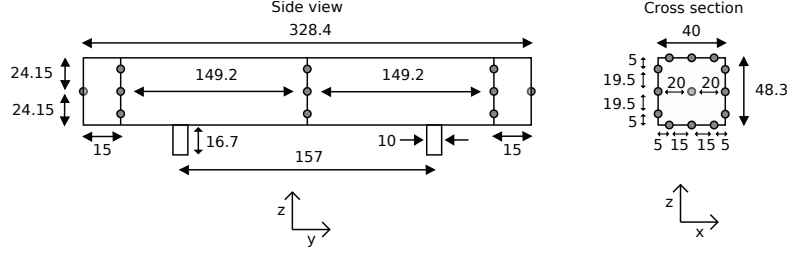


Figure 1.2.5: The dimensions of the train body and the distances between the measurement points. All numbers are given in [mm].

the rail on which the train travels. The dimensions of the wind tunnel nozzle and the ground board can be seen in figure 1.2.6.

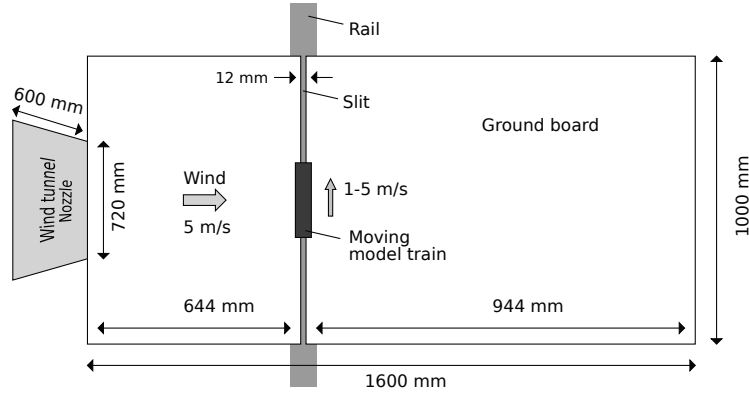


Figure 1.2.6: The dimensions in the experimental setup.

The experimental setup does obviously have several features that differs from the flow in real train scenarios:

- The model is a miniatur, hence the Reynolds number will become smaller and the flow less turbulent. This can influence important flow features such as separation points etc. However for a cuboid geometry, the flow will separate at the sharp edges for a wide range of Reynolds numbers.
- The velocity of the train is very low compared to real trains ( $1-5 \text{ m/s} = 3.6-18 \text{ km/h}$ ), which will further decrease the reynolds number. The low velocity also gives very large yaw angles which is not very common in real cases, at least not for high speed trains.
- The side wind is induced by a wind tunnel, which produces a flow that probably differs from the wind gusts occuring in nature.
- The model is a single box with sharp edges, although freigh wagons often have a very box-like shape, the front of the train is not likely to have sharp edges in real life.

This thesis aims primarily at comparing LES and PANS with the available experimental data, but the long term goal is to simulate a full scale model train. Before we proceed with larger simulations and experiments it is important to validate our simulation methods on generic cases. As said the low velocities and the small train body will lower the reynolds number and hence make a LES possible, because the mesh resolution is highly correlated with the reynolds number. The sharp edges of the train geometry ensures a well defined separation. This is good because it makes it easier to predict the flow, and it also makes the flow more Re independent. The experiment is therefore suitable to evaluate the LES and PANS models, since it is similar to reality but is simplified in a way that enables good simulations to be done. The scenarios studied in this thesis; constant yaw angle  $90^\circ$ , and the train passing the region of crosswind at  $5 \text{ m/s}$ , will from now on be refered to as *the stationary scenario*, and *the moving scenario*, respectively. Note however that the flow in the stationary scenario is highly transient, meaning that unsteady turbulent fluctuations are present at all times. But since the yaw angle  $90^\circ$  is constant in time, the time-averaged flow will converge to a steady state. For the moving case, a time average over the full scenario will be less meaningful, since the yaw angle is changing when



the train is entering and leaving the region of crosswind. The yaw angle will be constant ( $45^\circ$ ) during a small amount of time since the wind tunnel nozzle is wider than the train length, but it is not sufficient to make a time average meaningful.

### 1.3 Purpose

The purpose of this thesis is to evaluate the performance of PANS using  $\zeta$ - $f$  as RANS model. Reference LES will be performed on the same mesh. On a mesh too coarse to produce a fully resolved LES, can PANS provide a solution that is in better agreement to the experimental data? It is also interesting to compare the computational demands for PANS and LES, since PANS is using four closure equations.

For the moving case it is relevant to ask whether a moving velocity profile is sufficient to model a moving train passing a perpendicular side wind, which will be evaluated in the comparison with experimental data.

### 1.4 Limitations

Due to lack of time, a mesh dependence study is not performed for either of the two cases. This is a severe limitation since the mesh dependence is a highly relevant issue for most CFD-problems.

## 2 Theory

This chapter aims merely to be a short and shallow review of the most relevant theory that lies as a foundation for the simulations performed in this thesis.

### 2.1 Solving the incompressible Navier-Stokes equations

The famous Navier-Stokes equations (NS) reads in incompressible form, with tensor notation:

$$\frac{\partial U_i}{\partial t} + U_j \frac{\partial U_i}{\partial x_j} = -\frac{\partial P}{\partial x_i} + \nu \frac{\partial^2 U_i}{\partial x_j \partial x_j} \quad (2.1.1)$$

Where  $U_i$  is the velocity,  $P$  is the pressure and  $\nu$  is the kinematic viscosity. Also  $\nu = \mu/\rho$ , where  $\mu$  is the dynamical viscosity and  $\rho$  is the fluid density. A balance between the number of unknowns and equations can be obtained with the continuity equation:

$$\frac{\partial U_i}{\partial x_i} = 0$$

Analytical solutions to NS has been found only in simple, special cases of flow, and certainly not for 3D-dimensional aerodynamic problems. It is possible to solve NS in its original form with numerical methods, referred to as Direct Numerical Simulations (DNS). The problem with DNS is that in real life aerodynamics the flow is highly turbulent. This means that the solution of NS exhibits a chaotic behavior that gives rise to rotational structures, or eddies, of varying size.



Figure 2.1.1: *Turbulence in a water flow*

The size of these eddies are related to the well known dimensionless Reynolds number ( $Re$ );

$$Re = \frac{\rho U L}{\mu}$$

Where  $\rho$  is the fluid density,  $U$  the flow velocity,  $L$  the characteristic length (in aerodynamics often the height of the body), and  $\mu$  the dynamical viscosity.  $Re$  is the ratio between the inertial forces in the flow;  $\rho U^2 L^2$  and the viscous forces  $\mu U L$ . The higher  $Re$ , the more turbulence the flow exhibits. Let  $\eta$  denote the length scale of the smallest turbulent eddies, and  $\ell$  denote the length scale of the largest turbulent eddies. The theory of turbulence states that ratio between the smallest and largest eddies is of the order  $\ell/\eta \sim Re^{3/4}$  [12]. The computational domain where the DNS resides then needs to be of size  $\sim \ell$ , and the mesh needs to have cells as small as  $\sim \eta$ , in order to accurately represent the solution. Since the DNS also must be performed in 3D-dimensions to describe the flow, we would need  $\sim (\ell/\eta)^3 \sim (Re^{3/4})^3 \sim Re^{9/4}$  cells. For example the train simulations of a miniatyr train at small velocities in this thesis has  $Re \sim 10^4$ , rendering a mesh size of  $\sim 10^9$  cells, which would require a rather unrealistic amount of computational resources. The small cells also sets a restriction for the timestep used in the simulation. For simplicity, we can think of a fluid particle that travels in x-direction with velocity  $U$  through a mesh cell of length  $\Delta x$ . The time dimension is incremented with timestep

$\Delta t$ . The widely used numerical criteria based on the so called Courant-Friedrichs-Lewy (CFL) number is then stated as:

$$CFL = \frac{U \Delta t}{\Delta x} \leq 1$$

This criteria basically says that a fluid particle should not pass through more than one cell during a timestep. The fact that the timestep is proportional to the cell size further increases the computational demands for a DNS.

## 2.2 Averaged Navier-Stokes equations

A way to remove fluctuations and reduce the computational cost is to average the velocity field  $U_i$ , either time or in space. The averaging is done implicitly, meaning that we derive equations that describe the average field. An explicit averaging would correspond to computing all turbulent fluctuations and afterwards applying the averaging filter. This would not decrease the computational cost. When averaging, the velocity  $U_i$  is decomposed into an averaged part  $\bar{U}_i$ , which is resolved in the simulation, and an unresolved part  $u_i$ :

$$U_i = \bar{U}_i + u_i$$

Saying that the averaging filter is linear, equations for  $\bar{U}_i$  can be derived from NS and the continuity equation:

$$\frac{\partial \bar{U}_i}{\partial t} + \bar{U}_j \frac{\partial \bar{U}_i}{\partial x_j} = -\frac{\partial P}{\partial x_i} + \nu \frac{\partial^2 \bar{U}_i}{\partial x_j \partial x_j} - \frac{\partial \tau_{ij}}{\partial x_j} \quad (2.2.1)$$

$$\frac{\partial \bar{U}_i}{\partial x_i} = 0$$

Where  $\tau_{ij} = \overline{u_i u_j} + \bar{u}_i \bar{u}_j$  is the subfilter stress tensor. In the Reynolds Averaged Navier Stokes, or RANS-approach the average is taken over such a period of time that the solution converges to a steady state (this of course assumes stationary boundary conditions). The mean velocity fluctuation therefore becomes zero:  $\bar{u}_i = 0$ , the subfilter stress is reduced to  $\tau_{ij} = \overline{u_i u_j}$  and is referred to as the Reynolds stresses. The subfilter (or Reynolds) stresses introduce new unknowns in the system of equations, and they must hence be modelled. The widely used Boussinesq assumption states that the unresolved stresses  $\tau_{ij}$  should be proportional to the average rate of strain  $S_{ij}$ :

$$S_{ij} = \frac{1}{2} \left( \frac{\partial \bar{U}_i}{\partial x_j} + \frac{\partial \bar{U}_j}{\partial x_i} \right) \quad (2.2.2)$$

$$\tau_{ij} = -2\nu_t S_{ij} + \frac{2}{3} k \delta_{ij} \quad (2.2.3)$$

Where  $\nu_t$  is invented and named the turbulent viscosity, or eddy viscosity, as an analogy to the fluid viscosity  $\nu$ . The turbulent kinetic energy is defined as  $k = \frac{1}{2} \overline{u_i u_i} = \frac{1}{2} (\overline{u_1^2} + \overline{u_2^2} + \overline{u_3^2})$ . Another quantity is introduced, namely the dissipation of turbulent kinetic energy  $\varepsilon$ , which is defined as the rate of destruction of  $k$ . The turbulent viscosity can be calculated on dimensional grounds as:

$$\nu_t = c_\mu \frac{k^2}{\varepsilon} \quad (2.2.4)$$

Where  $c_\mu$  is a dimensionless empirical constant.  $k$  and  $\varepsilon$  are assigned their own transport equations which are also derived with dimensional analysis and tuned with experimental parameters. The additional equations used to close the underdetermined system of equations given by Eq. 2.2.1 is called the *closure equations*. Since the RANS seeks a stationary solution to Eq. 2.2.1 the time-dependent part  $\partial \bar{U}_i / \partial t$  becomes zero, which is convenient since one does not have to consider any time integration. Instead the solution will converge to a time average which is often what one is interested in anyway. The time averaged solution removes all the small turbulent fluctuations and hence it is possible to use a very coarse mesh for RANS, compared to the mesh required for DNS. RANS is therefore very popular in industrial applications, and a large number of different RANS models has been proposed. A way to resolve is to retain the time dependant terms in the RANS equations. This method is called unsteady RANS (URANS), and it will resolve the largest frequencies of the time dependant flow while modelling the rest. Which time and length scales that will be resolved depends on the RANS-model

that is used. It is the modelled turbulent viscosity  $\nu_t$  that will dampen the turbulent fluctuations, and the magnitude of  $\nu_t$  depends on the model. A and a very dissipative RANS-model, like the standard  $k$ - $\varepsilon$ -model, will hardly resolve any turbulent flutuations at all, depending on the specific flow situation [4]. A way to reduce the dissipation in an URANS-simulation is to prescribe a very low value  $k$  at the inlet boundaries, and prescribe  $\varepsilon$  so that  $\nu_t \ll \nu$ . A better way to control the dissipation in the RANS-modeling is to use the Partially Averaged Navier Stokes (PANS) method. In PANS the ratio between the unresolved and total turbulence kinetic energy can be controlled directly by introducing new parameters in the RANS-equations. The aim is then to resolve as much turbulence as possible give the resolution in the mesh, and to use a RANS model for the unresolved turbulence.

## 2.3 PANS

The concept of Partially Averaged Navier Stokes (PANS) equations introduces the parameters  $f_k$  and  $f_\varepsilon$ , which are defined as the ratio between the unresolved and total kinetic energy ( $f_k$ ) and dissipation ( $f_\varepsilon$ ). Setting  $f_k = f_\varepsilon = 1$  should turn PANS into URANS, while  $f_k = f_\varepsilon = 0$  will retain the original NS (Eq. 2.1.1). The early PANS method proposed by Girimaji in [5] was based on the standard  $k$ - $\varepsilon$  model, while in this thesis the  $\zeta$ - $f$  model is used. This was first proposed by Basara, Krajnović and Girimaji in [2]. A weakness in the RANS model will naturally be inherited by its PANS counterpart, hence the  $\zeta$ - $f$ -model is a good choice. The  $\zeta$ - $f$  model is developed to correct the inaccurate near wall behavior of the  $k$ - $\varepsilon$ -model, as well as being robust to insufficient mesh resolution near the wall [6]. In  $\zeta$ - $f$ , the transport equations for  $k$  and  $\varepsilon$  are still used, but an additional normalised wall-normal velocity scale  $\zeta$  is introduced.  $\zeta$  is defined as  $\zeta = \overline{v^2}/k$ , where  $v$  can be thought of as the wall-normal turbulent velocity fluctuations.  $f$  is an elliptic relaxation function that adjusts the behavior of  $\zeta$  close to the wall.  $\zeta$  is incorporated in the equation for turbulent viscosity (2.2.4):

$$\nu_t = c_\mu \zeta \frac{k^2}{\varepsilon}$$

In PANS, the turbulent kinetic energy and dissipation is divided into resolved parts  $k_r$  and  $\varepsilon_r$ , and unresolved parts  $k_u$  and  $\varepsilon_u$ :

$$k = k_r + k_u, \quad \varepsilon = \varepsilon_r + \varepsilon_u$$

$f_k$  and  $f_\varepsilon$  is then defined as the unresolved to total ratio of  $k$  and  $\varepsilon$ :

$$f_k = \frac{k_u}{k}, \quad f_\varepsilon = \frac{\varepsilon_u}{\varepsilon} \quad (2.3.1)$$

The large majority of the dissipation is expected to take place at the smallest scales, which we don't want to resolve. Therefore  $f_\varepsilon = 1$  is a reasonable assumption. The equations for the unresolved quantities  $k_u$ ,  $\varepsilon_u$ ,  $\zeta_u$  and  $f_u$  can be derived by combining definition 2.3.1 with the original  $\zeta$ - $f$ -equations, yielding the following:

$$\frac{\partial k_u}{\partial t} + \overline{U}_j \frac{\partial k_u}{\partial x_j} = \frac{\partial}{\partial x_j} \left[ \left( \nu + \frac{\nu_u}{\sigma_{ku}} \right) \frac{\partial k_u}{\partial x_j} \right] + P_u - \varepsilon_u \quad (2.3.2)$$

$$\frac{\partial \varepsilon_u}{\partial t} + \overline{U}_j \frac{\partial \varepsilon_u}{\partial x_j} = \frac{\partial}{\partial x_j} \left[ \left( \nu + \frac{\nu_u}{\sigma_{\varepsilon u}} \right) \frac{\partial \varepsilon_u}{\partial x_j} \right] + C_{\varepsilon 1} \frac{\varepsilon_u}{k_u} P_u - C_{\varepsilon 2}^* \frac{\varepsilon_u}{k_u} \varepsilon_u \quad (2.3.3)$$

$$\frac{\partial \zeta_u}{\partial t} + \overline{U}_j \frac{\partial \zeta_u}{\partial x_j} = \frac{\partial}{\partial x_j} \left[ \left( \nu + \frac{\nu_u}{\sigma_{\zeta u}} \right) \frac{\partial \zeta_u}{\partial x_j} \right] - \frac{\zeta_u}{k_u} P_u + \frac{\zeta_u}{k_u} (1 - f_k) \varepsilon_u + f_u \quad (2.3.4)$$

$$L_u^2 \nabla^2 f_u - f_u = \frac{1}{T_u} \left( c_1 + C_2' \frac{P_u}{\varepsilon_u} \right) \left( \zeta_u - \frac{2}{3} \right) \quad (2.3.5)$$

Where  $P_u$  is said to be the production of unresolved turbulent kinetic energy, which is modelled as:

$$P_u = 2\nu_u S_{ij} \frac{\partial \overline{U}_i}{\partial x_j}$$

$T_u$  and  $L_u$  is the unresolved taylor time- and length scale:

$$T_u = \max \left[ \min \left[ \frac{k_u}{\varepsilon_u}, \frac{0.6}{\sqrt{6}|S|\zeta_u} \right], C_\tau \sqrt{\frac{\nu_u}{\varepsilon_u}} \right]$$

$$L_u = C_L * \max \left[ \min \left[ \frac{k_u^{3/2}}{\varepsilon_u}, \frac{k^{1/2}}{\sqrt{6}|S|\zeta_u}, C_\tau \sqrt{\frac{\nu_u}{\varepsilon_u}} \right] \right]$$

$f_k$  regulates the turbulent diffusion of  $k_u$  and  $\varepsilon_u$  by adjusting the constants  $\sigma_{ku,\varepsilon u}$ :

$$\sigma_{ku,\varepsilon u} = \sigma_{k,\varepsilon} f_k^2 \quad (2.3.6)$$

$f_k$  also regulates the parameter  $C_{\varepsilon 2}^*$ , which is taken as:

$$C_{\varepsilon 2}^* = C_{\varepsilon 1} + f_k(C_{\varepsilon 2} - C_{\varepsilon 1}) \quad (2.3.7)$$

The other parameters are empirically derived constants for the  $\zeta$ - $f$ -model, which value are shown in tabel 2.3.1 below.

Table 2.3.1: Constants used in the  $\zeta$ - $f$ -model.

$C_\mu$	$C_{\varepsilon 1}$	$C_{\varepsilon 2}$	$c_1$	$C_2'$	$\sigma_k$	$\sigma_\varepsilon$	$\sigma_\zeta$	$C_\tau$	$C_L$	$C_\eta$
0.22	1.4	1.9	0.4	0.65	1	1.3	1.2	6.0	0.36	85

The unresolved stress  $\tau_{ij}$  in the averaged NS (equation 2.2.1) is computed as before:

$$\tau_{ij} = -2\nu_u S_{ij} + \frac{2}{3}k_u \delta_{ij}$$

Where  $\nu_u$  is the eddy viscosity of the unresolved scales:

$$\nu_u = c_\mu \zeta_u \frac{k_u^2}{\varepsilon_u}$$

$S_{ij}$  is the resolved rate of strain, or stress tensor, as given in equation 2.2.2. Now,  $f_k$  could be set beforehand to a constant value in the simulation, but in the current PANS model  $f_k$  is recomputed at the beginning of every timestep as proposed in [3].

$$f_k = \frac{1}{\sqrt{C_\mu}} \left( \frac{\Delta}{\Lambda} \right)^{2/3} \quad (2.3.8)$$

Where  $\Delta$  is the the local cell dimension (taken as the cube root of the cell volume) and  $\Lambda$  is the taylor length scale of turbulence:

$$\Lambda = \frac{k^{3/2}}{\varepsilon}$$

This is an attempt to compute the value of  $f_k$  so that the resolved turbulent length scale is of the same order as the local cell size. A derivation of this expression can be found in [5]. Since the computation of  $f_k$  depends on the total TKE  $k = k_u + k_r$ , the resolved TKE  $k_r$  need to be computed as well. According to the definition, the unresolved TKE  $k_u$  is modelling the partial average of the *unresolved* fluctuation:

$$2k_u = \overline{u_1^2} + \overline{u_2^2} + \overline{u_3^2}$$

Where  $u_i = U_i - \overline{U}_i$ . To find the *resolved* fluctuation we can apply a time average over the full simulation time on the resolved velocity  $\overline{U}_i$ , denoted as  $\langle \overline{U}_i \rangle$ . The resolved fluctuation  $u_{r,i}$  is approximated as  $u_{r,i} = \overline{U}_i - \langle \overline{U}_i \rangle$ , and  $k_r$  is computed from the full time average of  $u_{r,i}^2$ :

$$2k_r = \langle u_{r,1}^2 \rangle + \langle u_{r,2}^2 \rangle + \langle u_{r,3}^2 \rangle \quad (2.3.9)$$

This way of computing  $k_r$  assumes that  $\langle \overline{U}_i \rangle$  is a converged, stable average that will not change over time. If the boundary conditions are changed,  $\overline{U}_i$  might deviate from  $\langle \overline{U}_i \rangle$ , not as a turbulent fluctuation but as a change in the global flow conditions. Computing  $k_r$  in this way, all deviations from the total time average will

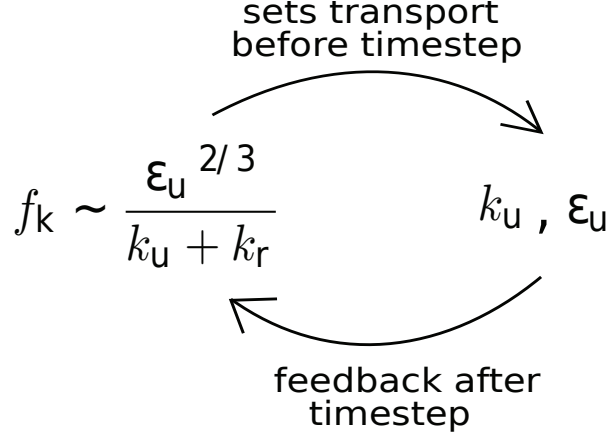


Figure 2.3.1: *The dynamic updating of  $f_k$*

be interpreted as turbulent fluctuations, which might not be true. The dynamic updating of  $f_k$  in Eq. 2.3.8 means that  $f_k$  will depend on the local value of  $k_r$ ,  $k_u$  and  $\epsilon_u$  before each time step:

$$f_k \sim \frac{\epsilon_u^{2/3}}{k_u + k_r}$$

This adds extra complexity to the model, which is illustrated in figure 2.3.1. Note that for a developed flow with stationary boundary conditions  $k_r$  should be more or less constant. Worth mentioning is also that is slightly deluding to define  $f_k$  as the ratio between unresolved to total ratio of turbulent kinetic energy. PANS is derived by assuming that  $k$  in the original URANS equations is the total TKE, but this is not true since URANS should resolve a non zero amount of TKE.  $f_k$  is rather the ratio between the TKE modelled by the URANS equations, and the TKE modelled by the PANS equations.

## 2.4 LES

Large Eddy Simulations, or LES, is like PANS aiming to resolve the large turbulent structures, or eddies, and to model the effect of the unresolved scales. The resolved velocity  $\bar{U}_i$  is however in LES thought of as a local volume average, instead of a partial time average. The specific model used in this thesis is called the standard Smagorinsky model [11]. LES is, like RANS and PANS, using the Boussinesq assumption to model the subfilter stress  $\tau_{ij}$ :

$$\tau_{ij} = -2\nu_{SGS}S_{ij} + \frac{1}{3}\delta_{ij}\tau_{ii}$$

Where  $\nu_{SGS}$  is called the sub-grid-scale(SGS) viscosity, SGS being another term for the unresolved scales. In LES the SGS viscosity is modelled using only a single algebraic equation:

$$\nu_{SGS} = (C_s\Delta)^2|S| \quad (2.4.1)$$

Where  $\Delta$  is the local filter width, naturally taken to be the local cell size, while  $C_s = 0.1$ . Without going in to details it is worth noting that equation 2.4.1 is based on the assumption that the production and dissipation of turbulent energy is in balance, which is a *good assumption only for the smallest turbulent eddies*. This means that the turbulent eddies must be resolved all the way down to the smallest scales, which puts severe demands on the mesh resolution. LES is of course substantially more economic than DNS, but lacks the flexibility of PANS which gradually can resort to URANS modelling when the mesh resolution decreases. It is however computationally cheaper than PANS on the same mesh, comparing 4 extra differential equations (2.3.2-2.3.5) against one algebraic (2.4.1).

## 2.5 Measuring mesh resolution at the wall

At the wall the no-slip condition says that the velocity is zero, and hence the velocity gradient is very large at the wall. The the mesh resolution at the wall is very important and needs to be quantified. The normalized wall

distance  $y^+$  can then be used:

$$y^+ = y \sqrt{\frac{1}{\nu} \frac{\partial u}{\partial y}} \bigg|_{y=0}$$

Where  $u$  is the velocity parallel to the wall and  $y$  is the wall normal distance.  $y^+$  is calculated at the node closest to the wall surface, and should there satisfy  $y^+ \leq 1$ , for both PANS and LES. Expressing the the streamwise and spanwise cellsize  $\Delta x$  and  $\Delta z$  in wall units;

$$\Delta x^+ = \Delta x \sqrt{\frac{1}{\nu} \frac{\partial u}{\partial y}} \bigg|_{y=0} \quad \Delta z^+ = \Delta z \sqrt{\frac{1}{\nu} \frac{\partial u}{\partial y}} \bigg|_{y=0}$$

We have the approximate criteria for a well resolved LES [4]:

$$\Delta x^+ \leq 100 \quad \Delta z^+ \leq 30$$

## 2.6 Aerodynamic Coefficients

When talking about the forces acting on a train, is useful to define dimensionless force coefficients, in order to compare experiments and simulations of different scales. The normalized force coefficients are defined as

$$C_s = \frac{F_x}{0.5 U_\infty \rho A_x}$$

$$C_d = \frac{-F_y}{0.5 U_\infty \rho A_y}$$

$$C_l = \frac{F_z}{0.5 U_\infty \rho A_z}$$

Where  $F_{x,y,z}$  is the actual forces, and  $A_{x,y,z}$  is the projected surface area in the x-,y-, and z-direction.  $U_\infty$  is the free stream velocity and  $\rho$  is the fluid density.  $C_{s,d,l}$  is referred to as the side, drag and lift force respectively. Note that the drag coefficient  $C_d$  is usually defined in the x-direction, while the side force coefficient  $C_s$  is usually defined in the y-direction. In this thesis however, the train travels in the positive y-direction, while the crosswind comes from the x-direction, hence the definitions.

### 3 Method

#### 3.1 Computational domains and meshes

The geometry and the mesh is generated using the commercial software package ICEM-CFD. ICEM-CFD enables good control of the resolution near the train surface, as well as the stretching of the hexagonal cells further away from the walls. Figure 3.1.1 shows the dimensions of the computational domains used in both scenarios.  $H$  refers to the train height, and the convention is to have around  $8H$  upstream of the body and  $19H$  downstream. The requirements for the distances perpendicular to the free stream are not as large, and are often determined of the size of the wind tunnel if experiments are available. For the stationary scenario, the dimensions are based on the size of the ground board and the height of the wind tunnel nozzle. The upstream distance and the height could probably be decreased to lower the size of the mesh, as done in the domain used for the moving scenario. The distance on the east lee side of the train is only  $15H$  for the moving scenario since the yaw angle will be only  $45^\circ$  when the crosswind is applied. The separated flow region on the lee side of the train is therefore not expected to travel as far in the x-direction as when the yaw angle is  $90^\circ$ . In the stationary scenario the reynolds number is calculated to:  $Re = \frac{U_\infty H}{\nu} = \frac{7 * 0.0483}{1.51 \cdot 10^{-5}} \approx 16000$ . The

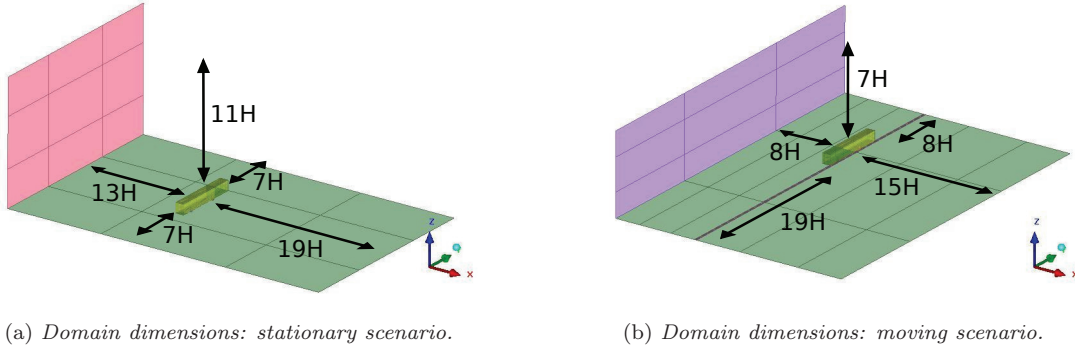
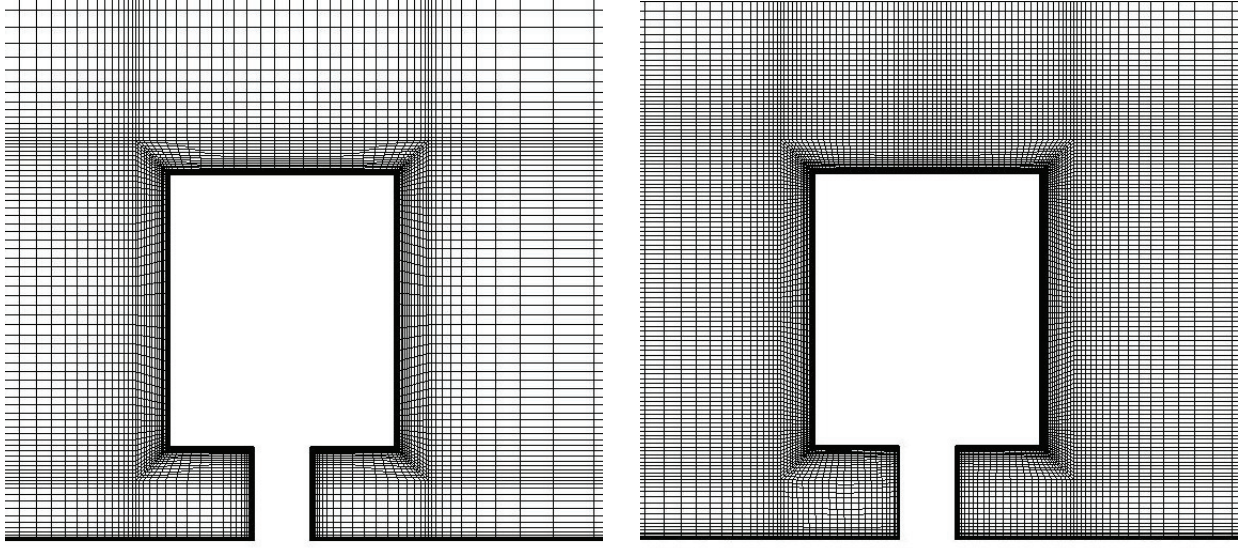


Figure 3.1.1: *Dimensions of the computational domains.*

$Re$  for the moving scenario is higher since it must be based on the maximum effective crosswind speed  $\approx 7$  m/s:  $Re = \frac{U_\infty H}{\nu} = \frac{7 * 0.0483}{1.51 \cdot 10^{-5}} \approx 23000$ . With the higher  $Re$  the mesh (see section 2.1) need substantially higher resolution for LES to resolve the flow. For the moving case the flow is changing directions which also put demands on the mesh resolution, since the it must always be high in the spanwise direction (parallel to the surface but perpendicular to the flow). Therefore the mesh for the stationary scenario has 5.4 million cells, while for the the moving scenario 13.3 million cells is used. Mesh planes in the vicinity of the train body is displayed in figure 3.1.2, looking from the front of the train, and in figure 3.1.3, from a side view. Note the difference in spatial resolution.

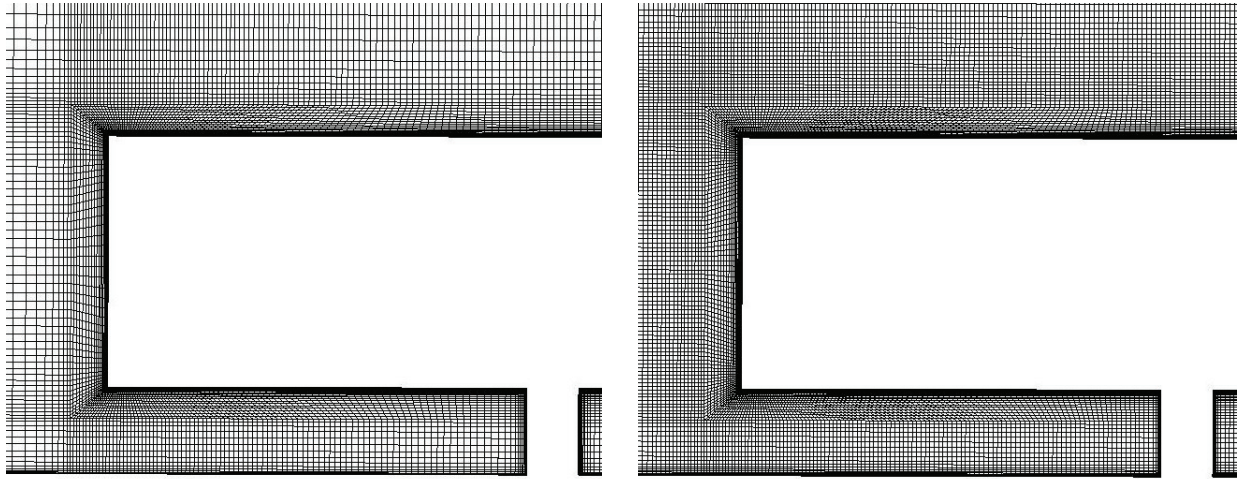




(a) *Mesh plane: stationary scenario.*

(b) *Mesh plane: moving scenario.*

Figure 3.1.2: *Mesh regions seen from the front of the train. The crosswind will approach from the right side.*



(a) *Mesh plane: stationary case.*

(b) *Mesh plane: moving case.*

Figure 3.1.3: *Mesh regions seen from the side of the train. The crosswind will flow into the plane.*

## 3.2 Boundary conditions modelling a stationary train in crosswind

The boundary conditions used for modelling the stationary yaw angle  $90^\circ$  is set according to conventions. The west boundary, which is the inlet, is assigned a normal velocity component of magnitude 5 m/s. No gradients in the flow are expected at the side walls and the roof, and they are treated as symmetry planes. This will resemble the open space in the experiment. On the east boundary wall, which is the outlet, a homogeneous neumann boundary condition is applied, meaning that the velocity gradient  $\nabla U = 0$ . This will let the flow pass through the outlet without affecting the upstream flow, provided that the upstream distance to the aerodynamic body is large enough. The no-slip condition, meaning  $U_i = 0$  is set on the train as well as on the floor. The boundary conditions are schematically represented in figure 3.2.1.

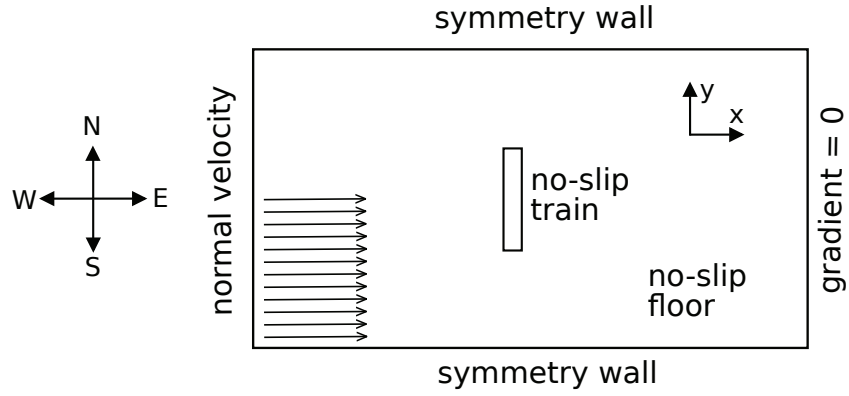


Figure 3.2.1: *Schematic representation of the boundary conditions for the stationary scenario. The symmetry roof is excluded for simplicity.*

### 3.3 Boundary conditions modelling a moving train in crosswind

In the experimental setup the train is moving, entering and passing the region of crosswind generated from the wind tunnel. In the simulation the train is stationary, but the crosswind velocity profile is moving instead. To impose the proper massflow in the cross direction of the train movement, i.e the x-direction, the velocity profile is applied on both sides of the train, east as well as west. A schematic illustration of the boundary conditions on the east and west wall are shown in figure 3.3.1

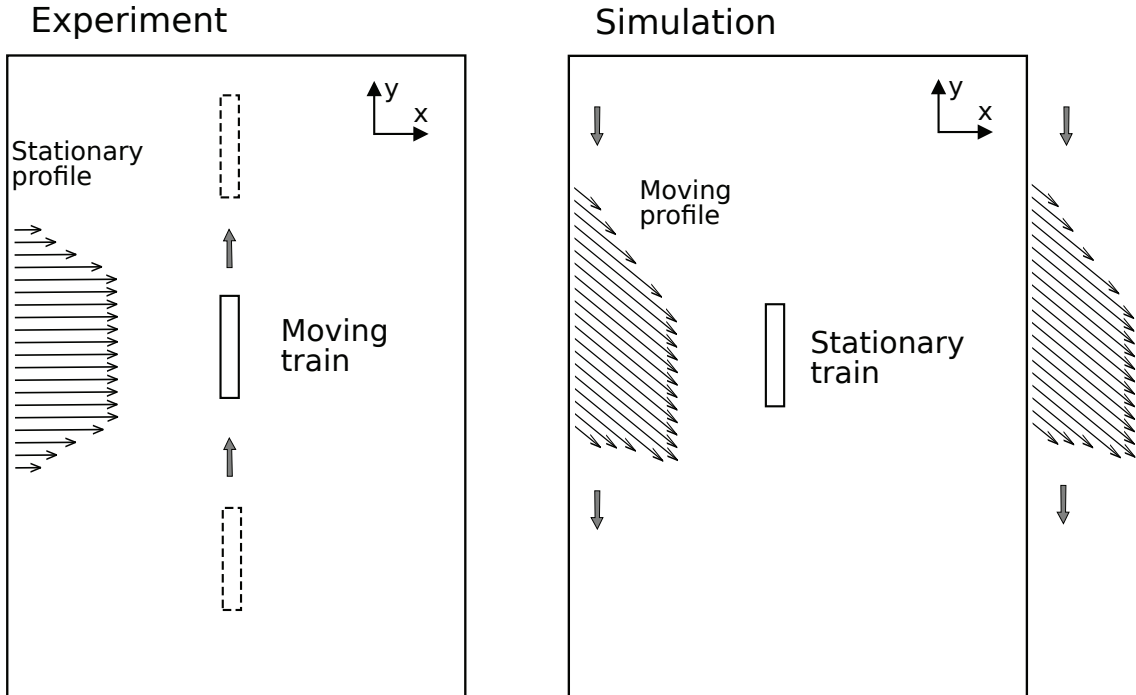


Figure 3.3.1: *Schematic illustration comparing the experimental setup with the simulation. Note that, for simplicity, only the boundary conditions at the side inlet and outlet (west and east) are included.*

Note that it is important to prescribe the crosswind velocity profile also on the north inlet, which is facing the front of the train. This makes sure that the crosswind is propagated through the entire domain in x-direction already when the profile is entering the domain. The south outlet is set as  $\nabla U = 0$ , in order to affect the flow as

little as possible. The east outlet could have been set to  $\nabla U = 0$ , but instead the crosswind profile is prescribed there. This makes sure that the proper massflow is given in the x-direction, but it forces the velocity field to be identical at the west inlet and east outlet, which is unphysical. However this the flow conditions on the lee side will not affect the flow around the train as much as the flow on the wind side. Putting the train far away from the east outlet hopefully makes the unphysical effects negligible, but it is a possible source of error. The moving velocity profile is moving with the negative train velocity, i.e. -5 m/s in the y-direction. The y-component of the velocity:  $U_2 = V = -5$  m/s is therefore prescribed on the north inlet (as a normal component), as well as the west inlet and the east outlet (as a tangential component). The no-slip floor must also be prescribed the negative train velocity, making it a "moving floor". Figure 3.3.2 is an attempt to give a full picture of the boundary conditions:

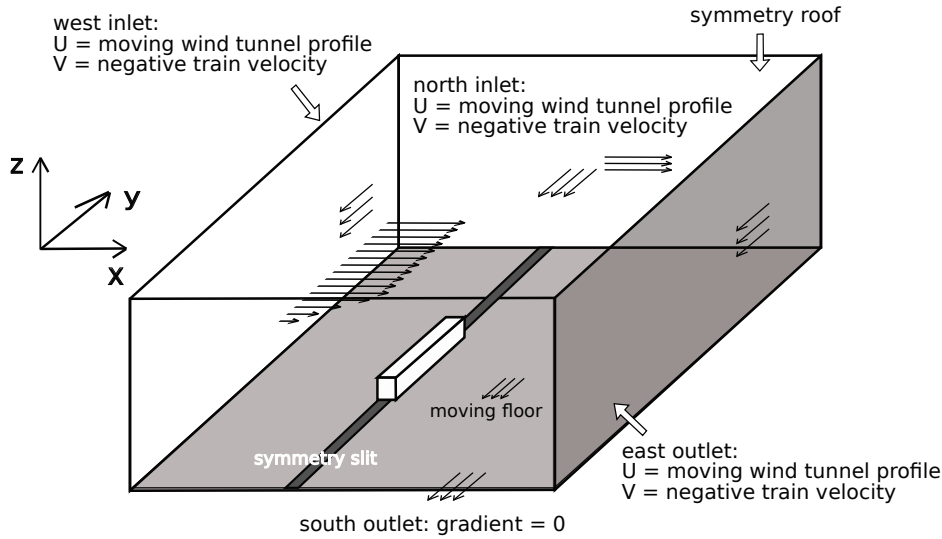


Figure 3.3.2: *Schematic illustration of the boundary conditions for the moving scenario.*

In the experiment there is a slit in the ground board, where the cylinders continues down to the carriage which brings the train forward. To resolve this kind of cavity flow is probably a thesis project in itself, why instead the ground slit is set as a symmetry plane. Physically this would signify that the train has a mirrored copy of itself below the ground board, which is of course not true. However it should simulate a resemblance of an open space in the ground slit. The top roof of the domain is set as a symmetry plane as well, according to conventions. Velocity data for the windtunnel profile are available from the experiments, obtained by removing the train model from the ground plate and measuring the crosswind speed. The velocity is measured at 19 locations along the y-direction, keeping the x- and z-position constant in the center of the train crosssection. The velocity data is not suitable to describe with a single polynomial, why instead spline interpolation is used. Spline interpolation corresponds to a 3rd order polynomial being fitted in between each adjacent data point. The function *spline* in matlab is used for this task. Figure 3.3.3 shows the spline fit together with the experimental data points, as well as the resulting yaw angle for the moving scenario.

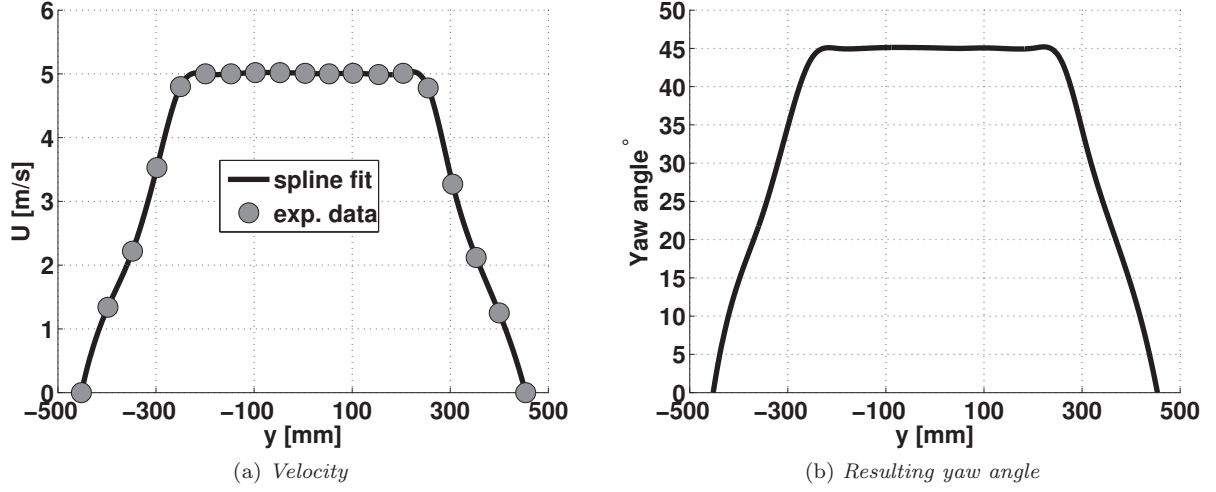


Figure 3.3.3: Spline fit of the experimental velocity data from the wind tunnel, and the resulting yaw angle for train speed 5 m/s.

## 3.4 Numerical setup

### 3.4.1 Numerical schemes and parameters

All simulations are implemented in the commercial CFD-package AVL Fire v2010. The numerical discretization is set as similar as possible for LES and PANS. For the spatial discretization; Central Differencing (C.D.) is used in the momentum and the continuity equation. In the finite volume code, the variables are stored only in the cell centers, but when solving the equations the values are needed at the cell faces as well. C.D. corresponds simply to a linear interpolation between two cell centers to evaluate the face between them. Using a 2nd order scheme is important since the accuracy needs to be high when describing small turbulent fluctuations. However, using C.D for the momentum equations (the filtered NS) can give rise to unphysical oscillations. The first order upwind scheme corresponds to evaluating the face value as equal to that of the upstream cell center. Since it is only first order accurate, this upwind scheme should hence not be used, but it is more stable than C.D. A common trick is to blend C.D. with upwind, i.e take a weighted average of the C.D value and the upwind value. Taking more than 5% of the upstream value is not recommended for a LES, which corresponds to an upwind blending factor of 0.95. For this thesis 0.98 is used for the momentum equation, while 1.0 is used for the continuity equation. For the  $\varepsilon_u$  and  $k_u$  equations the first order upwind scheme is used. It is generally desired to always use a 2nd order scheme, but the 1st order upwind scheme has the advantage of good convergence. For the time discretization a implicit second order scheme is used which is unconditionally stable, referred to as “2nd” in table 3.4.1. The timestep is  $\Delta t = 5 * 10^{-5}$  (5e-5) for all cases. The conventional SIMPLE algorithm is used to solve the coupled equations, where several iterations are performed in each timestep to ensure convergence. The under relaxation factors (URF:s) determines how much of the value in the previous inner iteration will be used in the next. The URF:s have to be tuned for each individual simulation while monitoring the iterations. The numerical schemes and parameters are given for both scenarios in table 3.4.1 and 3.4.2, as [LES value]/[PANS value].

Table 3.4.1: LES/PANS numerics: stationary scenario

Equation	Spatial Scheme	Upwind blending	Temporal Scheme	$\Delta t$	URF
Momentum	C.D/C.D	0.98/0.98	2nd/2nd	5e-5/5e-5	0.4/0.35
Continuity	C.D/C.D	1.0/1.0	2nd/2nd	5e-5/5e-5	0.4/0.35
$k_u$	- /upwind	- / -	2nd/2nd	5e-5/5e-5	- /0.4
$\varepsilon_u$	- /upwind	- / -	2nd/2nd	5e-5/5e-5	- /0.4

Table 3.4.2: LES/PANS numerics: moving scenario

Equation	Spatial Scheme	Upwind blending	Temporal Scheme	$\Delta t$	URF
Momentum	C.D/C.D	0.98/0.98	2nd/2nd	5e-5/5e-5	0.7/0.5
Continuity	C.D/C.D	1.0/1.0	2nd/2nd	5e-5/5e-5	0.7/0.5
$k_u$	- /upwind	- / -	2nd/2nd	5e-5/5e-5	- /0.5
$\varepsilon_u$	- /upwind	- / -	2nd/2nd	5e-5/5e-5	- /0.5

### 3.4.2 Initialization and averaging

The iterative time marching need to start at some point, why all the values in the domain need to be initialized. For all cases, this is done by setting  $U_\infty = U_y(t = 0) = 5m/s$  in all cells at the beginning of the first timestep. The velocities in the 2 other coordinate directions are set to zero:  $U_{x,z}(t = 0) = 0$ . This solution is highly unphysical, but the boundary conditions should "force" the flow to become realistic as the time marching proceeds. From the beginning of the simulation, the forces acting on the train ( $F_x$ ,  $F_y$  and  $F_z$ ) are monitored. When the flow is fully developed, the forces should oscillate around stable average values. The averaging of the flow should not be initialized before the flow is fully developed, since the initial solution does not represent the flow. How long the developed flow needs to be averaged depends on the magnitude of the lowest frequencies in the flow, i.e the frequency of the vortex shedding. For the stationary scenario, the flow is taken to be fully developed after 0.95 seconds, which corresponds to a fluid particle having passed the domain approximately 3 times. For LES, the total simulated time is 6 seconds while for PANS it is 5.5 seconds. This corresponds to the flow blowing through the domain 20 and 18.3 times respectively.

Unfortunately, due to a technical mistake the averaging is not taken from time  $t = 0.95$ , but instead from time  $t = 0.0$ . This means that the unphysical solution in the initial stages is included in the averaged results. The average results can hence not be fully trusted. However the simulations have been remade, and the results show that the proper averaged flow differs very little from the averaged flow presented in this thesis.

For the moving scenario, no averaging is done, but the flow is initialized to the negative train speed:  $U_x(t = 0) = 5m/s$  ( $U_{y,z} = 0$ ), and the flow is considered fully developed after 0.95 seconds. The moving velocity profile is then applied as a boundary condition, which will create a crosswind traveling in the x-direction through the domain, as described in section 3.3.



## 4 Results

### 4.1 Stationary Scenario: yaw angle $90^\circ$

#### 4.1.1 Instantaneous flow structures

Although the instantaneous flow should be highly chaotic, the presence of organized flow structures is important in many turbulent flows. A way to visualize these rotational structures is with an isosurface of  $Q$ ; the second invariant of the velocity gradient  $\nabla \bar{U}$ . The  $Q$ -surface can provide a good overall picture of the flow, and it makes it possible to compare the resolved turbulence in LES and PANS. The surface is colored with the normalized velocity magnitude  $|U|/U_\infty$ , where  $U_\infty = 5$  m/s is the free stream velocity. In Figure 4.1.1 we can see how the flow separates at the sharp edges of the train, forming the vortices that are responsible for the downstream wake region.

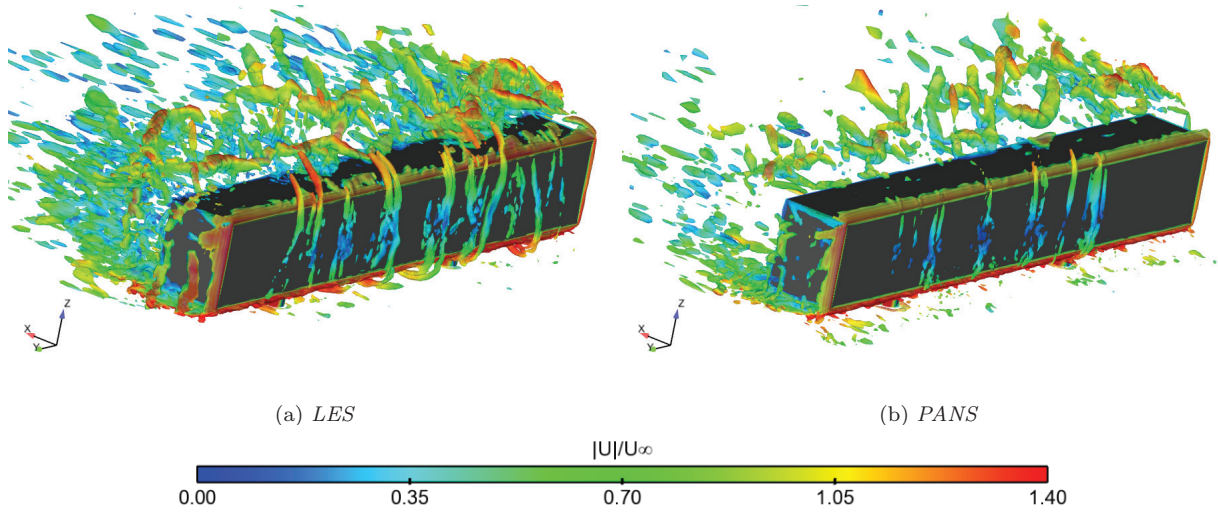


Figure 4.1.1: *Instantaneous flow structures around the train body, visualized by a  $Q$ -surface, colored by velocity.*

Figure 4.1.1 also shows that LES resolves smaller flow structures than PANS, which means that the dissipation that dampens out the unsteadiness in the momentum equations is larger in PANS. Large dissipation means a more averaged flow where instantaneous information will be lost. The question is whether enough of the important structures are captured and the unresolved turbulence is modelled in a good way.

### 4.1.2 CFL and $y^+$

Figure 4.1.2 shows instantaneous  $y^+$  for LES and PANS at the front and wind side of the train, where  $y^+$  has it's highest values. The vast majority of the values seem to satisfy  $y^+ \leq 1$ .

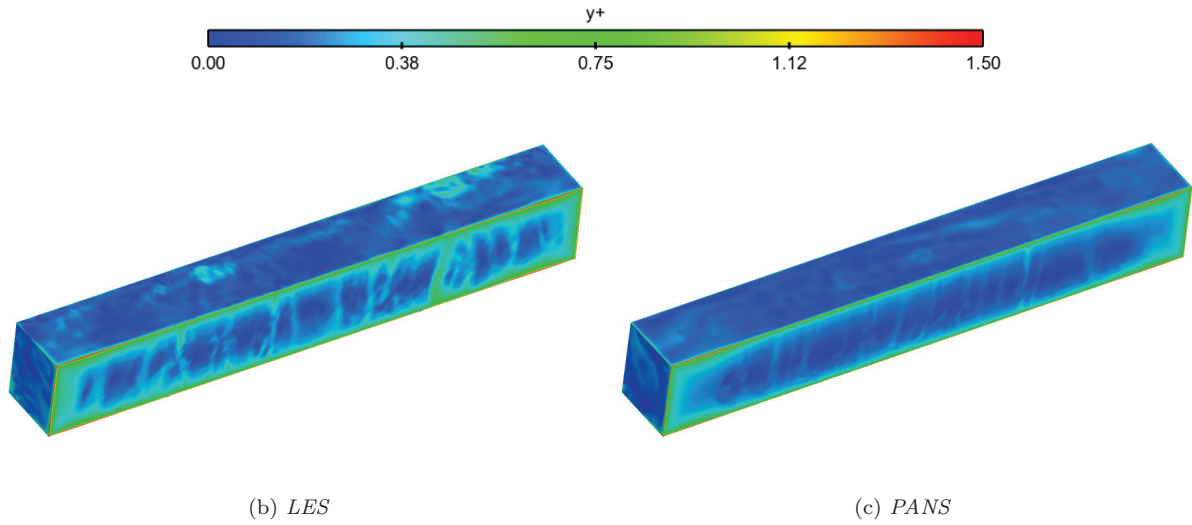


Figure 4.1.2: Train body colored with  $y^+$  values, the vast majority of the values appear to be close to or below unity.

In figure 4.1.3 we can see the the CLF number in a plane at mid height of the train. The CFL number seem to be well below one, which is desired.

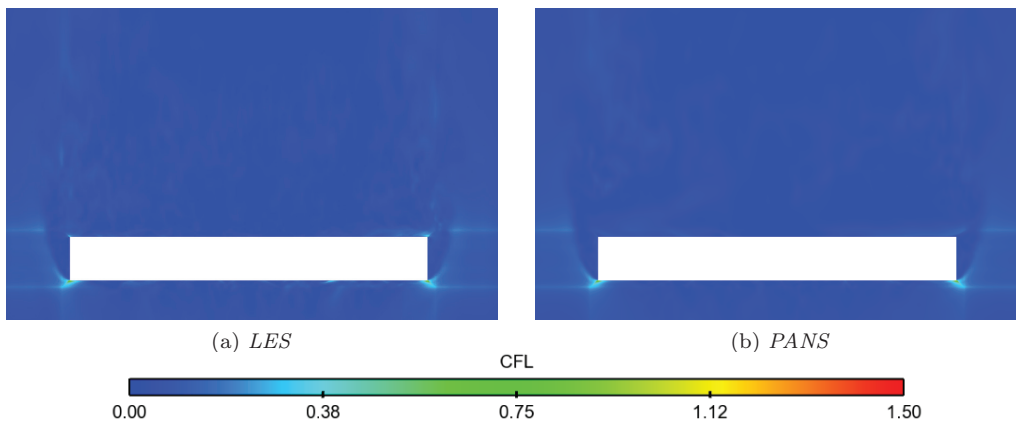


Figure 4.1.3: Train mid height plane colored with CFL number.

### 4.1.3 Validation with experimental pressure data

The average pressure is extracted from the train cross sections shown in figure 1.2.4 seen in section 1.2.1. The continuous pressure curves from LES and PANS can then be compared to the experimental data at the measurement points. The left graph in figure 4.1.4 shows the mid cross section at  $x = 0$ . The right graph shows a cross section at mid height of the train  $z/H=0.85$ . The pressure is given as the normalized pressure coefficient

$$C_p = \frac{P - P_{ref}}{0.5\rho U_\infty^2}$$

Where  $P$  is the computed pressure and  $P_{ref} = 10^5$  Pa is the reference pressure.

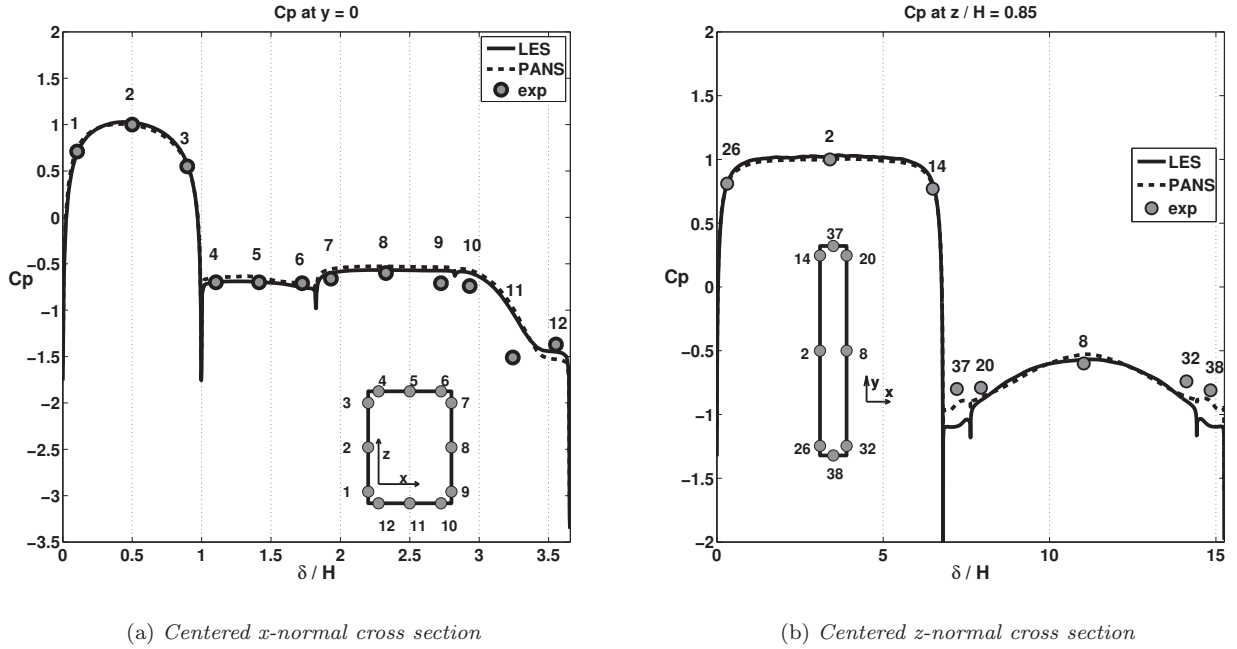


Figure 4.1.4: Comparison of LES, PANS and experimental data for the pressure coefficient  $C_p$ . Taken at centered crosssections from an  $y$ -normal backside view (a), and from an  $z$ -normal (b) above view.

At  $x = 0$  (4.1.4 (a)), LES and PANS is making a very similar prediction of the pressure, with a fairly good agreement to the experimental data. The pressure is slightly overpredicted at the bottom downstream end of the train (points 9-11). However looking at the the height centered cross section (4.1.4 (b)), LES is clearly failing by severely underpredicting the pressure at the lateral ends of the train (points 37-38). In comparison PANS is only doing a very slight underprediction. The reason why LES fails at the lateral edges could be that the flow there changes direction rendering  $z$  as the spanwise direction, see figure 4.1.5. The resolution of the mesh at the train surface is about 1.7 times coarser in the  $z$ -direction than in the  $y$ -direction. This could mean that the spanwise resolution is insufficient for LES at the lateral ends of the train. PANS utilises a more sophisticated modelling of the unresolved scales, and should be able to cope with a coarser spanwise resolution at the wall. The results indicate that this is the case. Figure 4.1.6 is showing the lateral cross sections near the back and the front of the train. Here PANS is doing a better job than LES at predicting the pressure at the roof of the train (points 16-18 and 28-30). Note that these cross sections should have identical pressure values, since the flow is symmetric around  $x = 0$ . PANS is predicting the pressure in better agreement with the experimental data than LES, but it is also more computationally demanding. PANS requires approximately 1.6 times as many cpu-hours as LES, for the same physical simulation time. PANS should also resolve the lowest frequencies of the flow, and hence needs the same averaging time as LES.



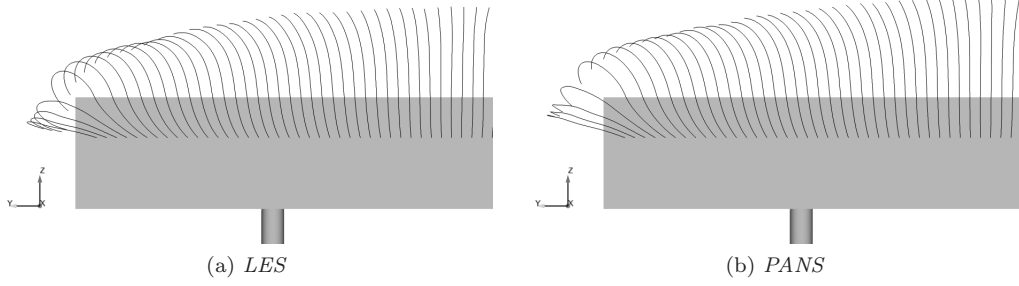


Figure 4.1.5: 3-dimensional streamlines emitted from a line at the wind side of the train. As expected the flow is directed in the lateral direction ( $y$ ) at the lateral end of the train.

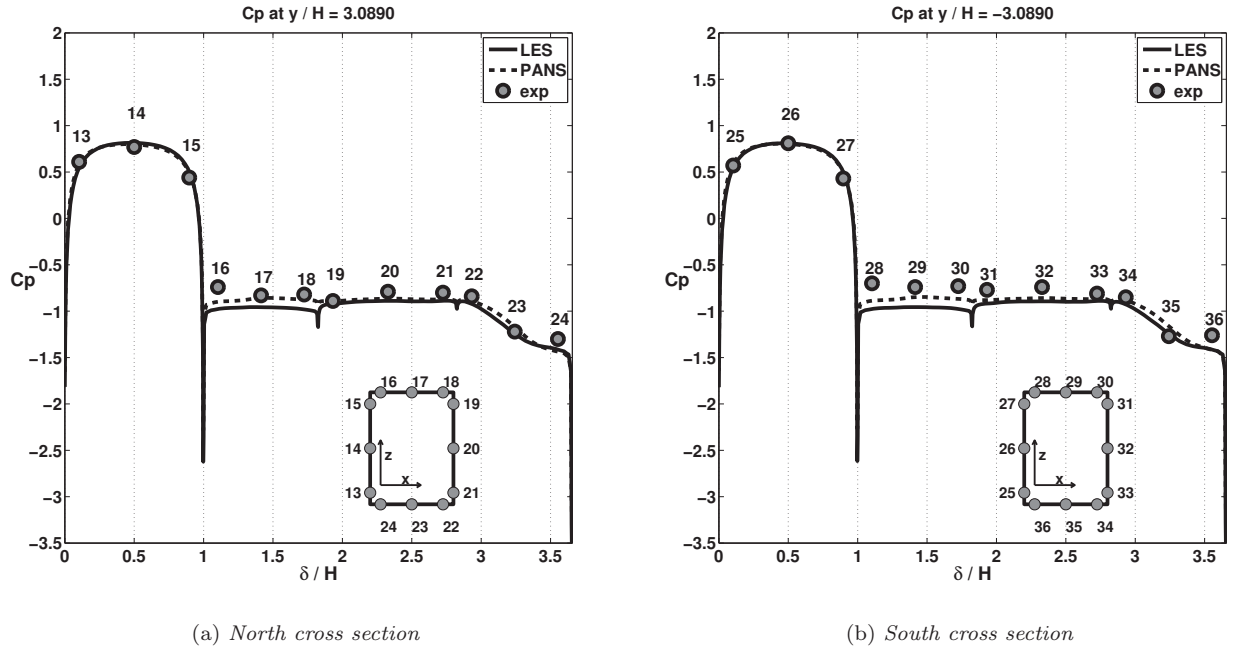


Figure 4.1.6: Comparison of *LES*, *PANS* and experimental data for the pressure coefficient  $C_p$  at the lateral crosssections.

#### 4.1.4 Force coefficients

We observe in figure 4.1.7 that the side force acting on the train is of roughly the same magnitude for LES and PANS. LES displays larger fluctuations, indicating a more unsteadiness in the flow, which naturally will produce higher magnitude peaks in the forces.

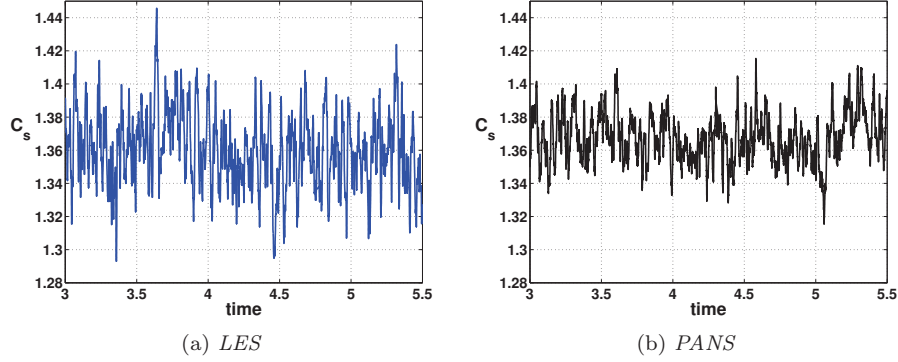


Figure 4.1.7: Side force coefficient  $C_s$ .

Figure 4.1.8 shows the lift coefficient  $C_l$ , which is in this case is negative. The lower lift predicted by PANS is consistent with figure 4.1.6 in section 4.1.3, where PANS predicted a higher pressure at the roof of the train.

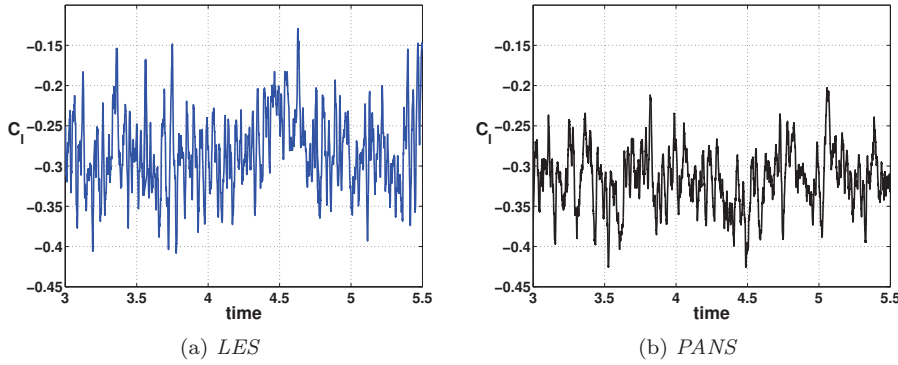


Figure 4.1.8: Lift force coefficient  $C_l$ .

Since the yaw angle is  $90^\circ$ , the average drag force should be zero, which is displayed in figure 4.1.9.

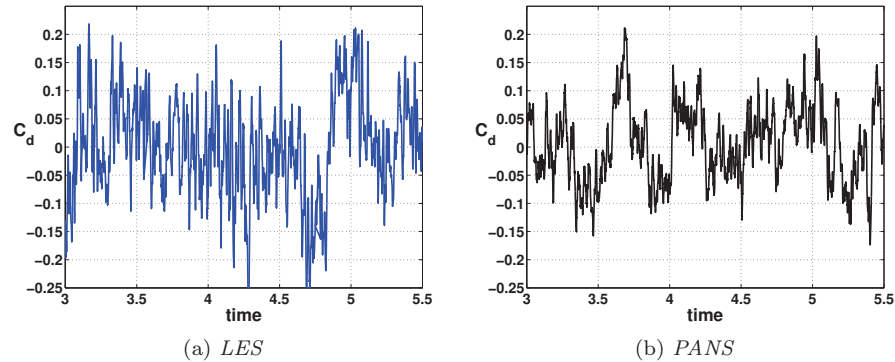


Figure 4.1.9: Drag force coefficient  $C_d$ .

### 4.1.5 Resolved and Unresolved Turbulence Kinetic Energy

As seen in section 4.1.1, figure 4.1.1, LES resolves smaller turbulent flow structures than PANS. This should mean that LES produces a larger resolved TKE  $k_r$  (see section 2.3, Eq. 2.3.9).  $k_r$  is compared for LES and PANS in figure 4.1.10.

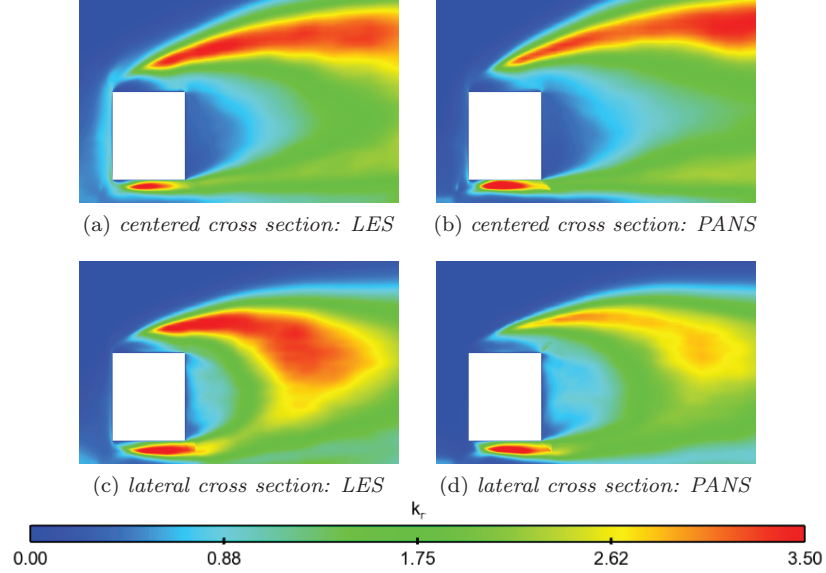


Figure 4.1.10: Comparing the resolved TKE  $k_r$  for LES and PANS.

LES has overall higher values of  $k_r$ , but the difference is larger at the lateral cross section, where LES failed to predict the pressure at the roof. PANS seem to behave more dissipative than LES on the current mesh. Therefore, PANS can be expected to produce a larger magnitude of unresolved TKE ( $k_u$ ) than LES. For LES  $k_u$  it is not explicitly used in the model equations, but it can be computed as  $k_u = k_{SGS} = C_s^2 \Delta^2 |S|^2 / 0.3$  (see chapter 2 for definitions).  $k_u$  is modelling the fluctuations from a partial time average, hence the instantaneous  $k_u$  field will be chaotic. To make the comparison easier, the total time average  $\langle k_u \rangle$  is considered instead.

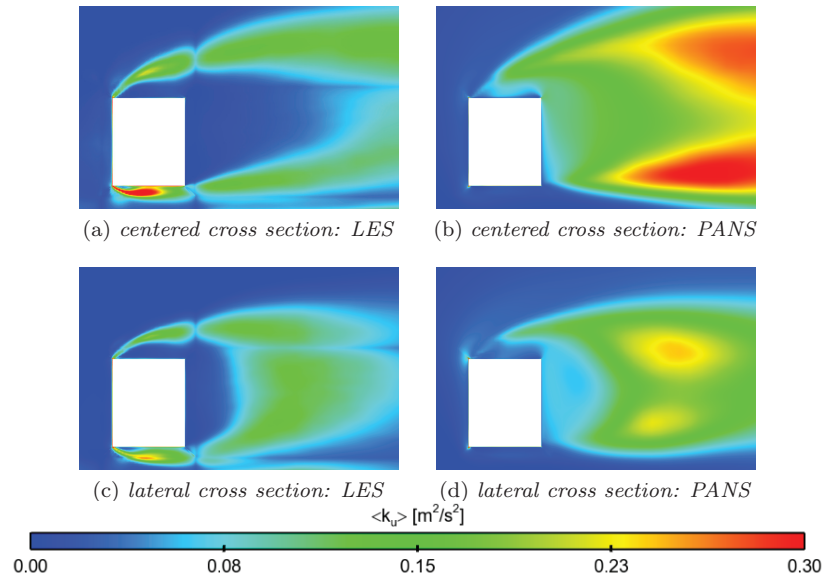


Figure 4.1.11: Averaged unresolved turbulence kinetic energy comparison between LES and PANS.

Figure 4.1.11 shows that PANS produces an overall larger amount of  $k_u$ , which means that it is modelling a larger fraction of TKE. To clarify further, the average unresolved to total ratio of TKE;  $\frac{\langle k_u \rangle}{\langle k_{tot} \rangle} = \frac{\langle k_u \rangle}{\langle k_u \rangle + \langle k_r \rangle}$  is visualized in figure 4.1.12. High values of the unresolved to total ratio should mean that the turbulence is

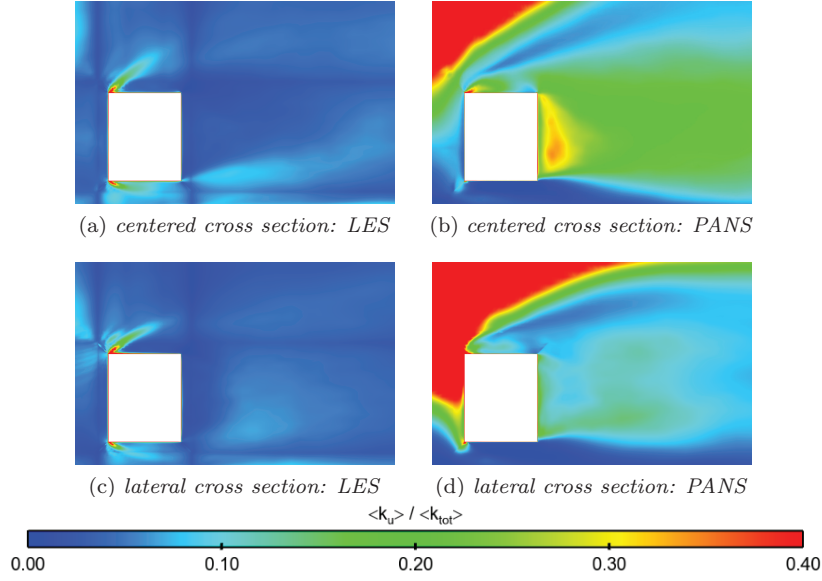


Figure 4.1.12: Averaged unresolved to total ratio of the turbulence kinetic energy:  $\frac{\langle k_u \rangle}{\langle k_u \rangle + k_r}$

modelled rather than resolved. For both models the ratio is rather small close to the train, but as expected PANS models a larger portion of  $k$  than LES. Together with the favorable pressure prediction this suggests that PANS works as intended; accurately modeling a larger portion of the turbulence hence decreasing the demands on mesh resolution. We want the modelling ratio to be larger for PANS than for LES, but it should not be too high. A ratio close to unity suggests a pure RANS modelling, which is not desired in the separated flow regions. One observation that raises questions is that under the train the ratio for PANS is close to zero. The pressure prediction here is also very similar to the LES prediction. The author has currently no suggestions why this is the case. Interesting is also to compare the *parameter*  $f_k$  to the *actual* ratio computed in the simulation, now denoted as  $F_k$ , where  $F_k = \frac{k_u}{k_u + k_r}$ .

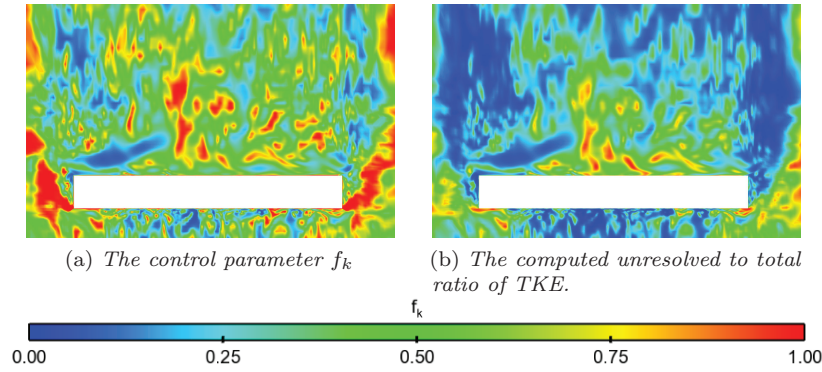


Figure 4.1.13: View from above comparing the control parameter  $f_k$  to the actual computed ratio  $F_k = \frac{k_u}{k_u + k_r}$ .

Figure 4.1.13 shows that the control parameter  $f_k$  is consistently higher than the computed ratio  $F_k$ , which is due to the fact that setting to  $f_k = 1$  will render an URANS- $\zeta$ - $f$  modeling with  $k_r > 0$ .

#### 4.1.6 Averaged flow field visualization

Since the instantaneous flow field is highly chaotic, it is convenient to study the averaged flow field instead. Figure 4.1.14 compares the time averaged streamlines for LES and PANS at the mid cross section where the pressure prediction is similar for both methods (see figure 4.1.4(a)). Even though the pressure prediction at the surface is very similar at the centered cross section, obvious differences can be observed when looking at the streamlines. PANS predicts more distinct separation and recirculation bubbles at the roof than LES. The

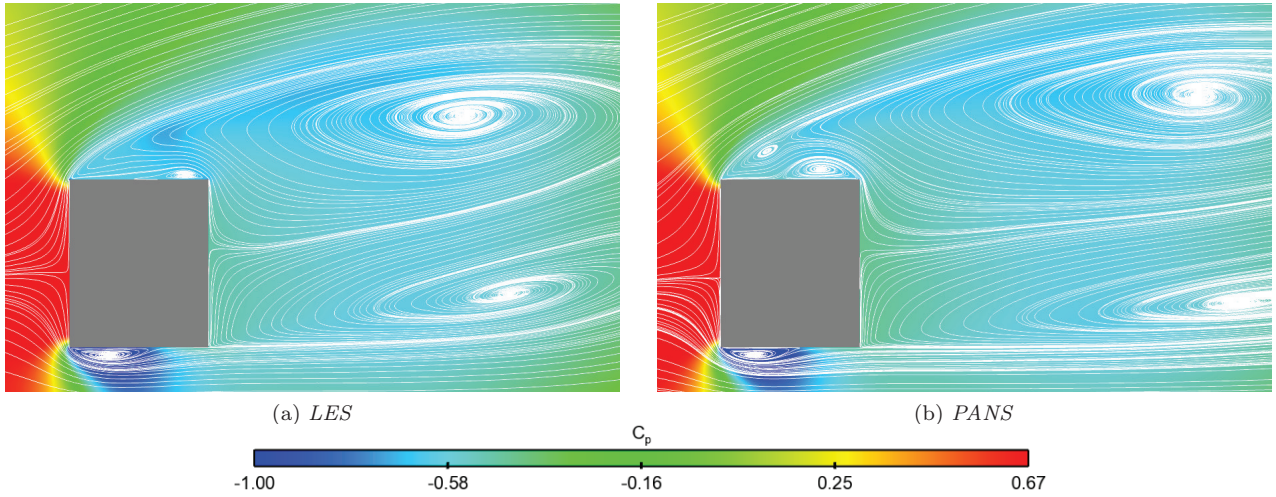


Figure 4.1.14: *Streamlines together with the averaged pressure field at the centered cross section.*

large recirculation regions forming behind the train also has a longer propagation in space. At the lateral cross sections, the flow is expected to be more different since the PANS predicted a higher pressure there (see figure 4.1.6). Figure 4.1.15 shows that PANS again is predicting a larger and more distinct separation at the roof, which is this case seem to affect the pressure prediction. A similar difference between LES and PANS

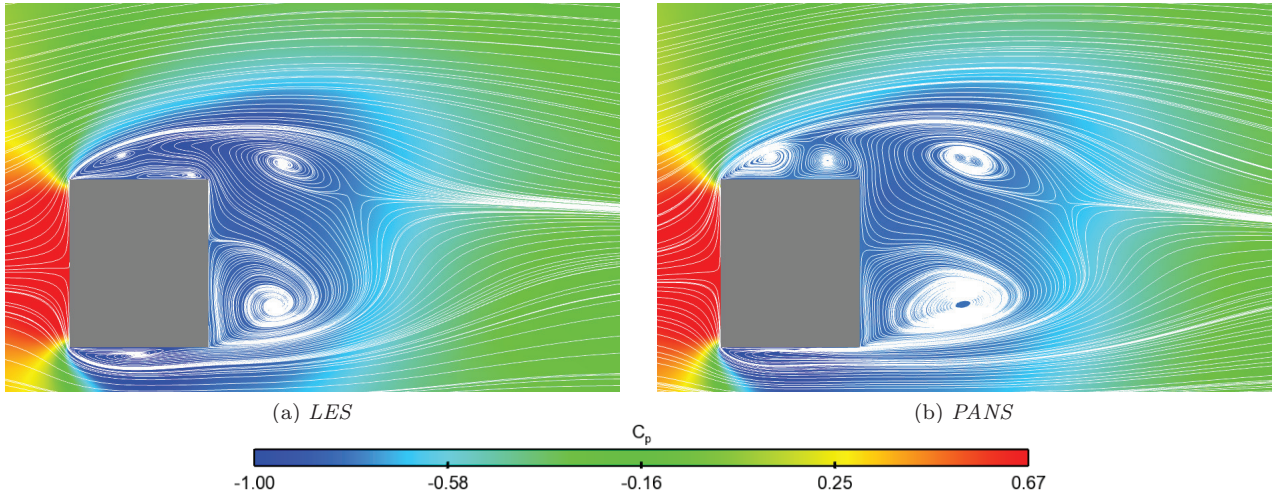


Figure 4.1.15: *Streamlines together with the averaged pressure field at one of the lateral cross sections.*

can be seen in figure 4.1.16 at the cross section seen from above, where LES is severely underpredicting the pressure (see figure 4.1.6(b)). A possible explanation for the higher pressure predicted from PANS is that the “second” recirculation bubble, following the separation bubble at the leading edge, is much more distinct in the flow predicted by PANS.



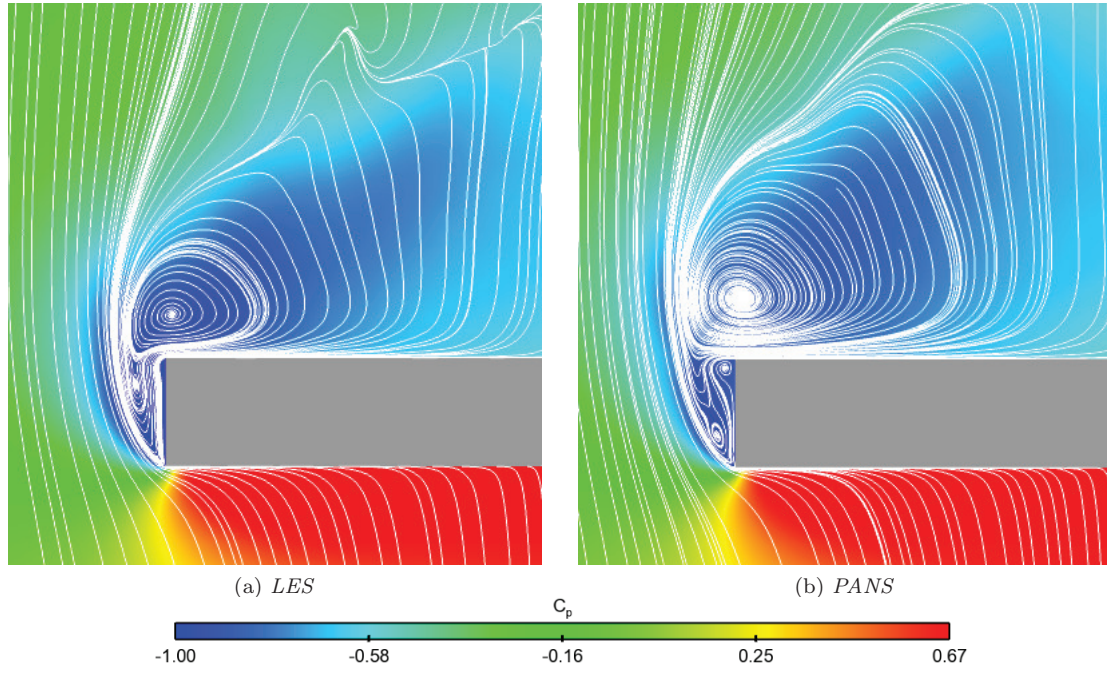


Figure 4.1.16: *Streamlines together with the averaged pressure field seen from above; plane at mid height of the train*

## 4.2 Moving Scenario: train speed 5 m/s

### 4.2.1 Visualization of the flow scenario

The moving scenario corresponds to the train traveling at a constant speed 5 m/s through the region of perpendicular side wind. The scenario is visualized in figure 4.2.1 for the LES simulation. The left column shows the velocity field in z-normal plane at mid height of the train, while the left column visualizes the flow structures with a Q-surface, and the pressure on the train surface. The difference between LES and PANS is less visible for the moving case, why only LES is displayed here. The sampling points  $y = -540, -220, -30, 280$ , and 680 mm refers to the position of the train midsection in relation to the center position of the cross wind profile.

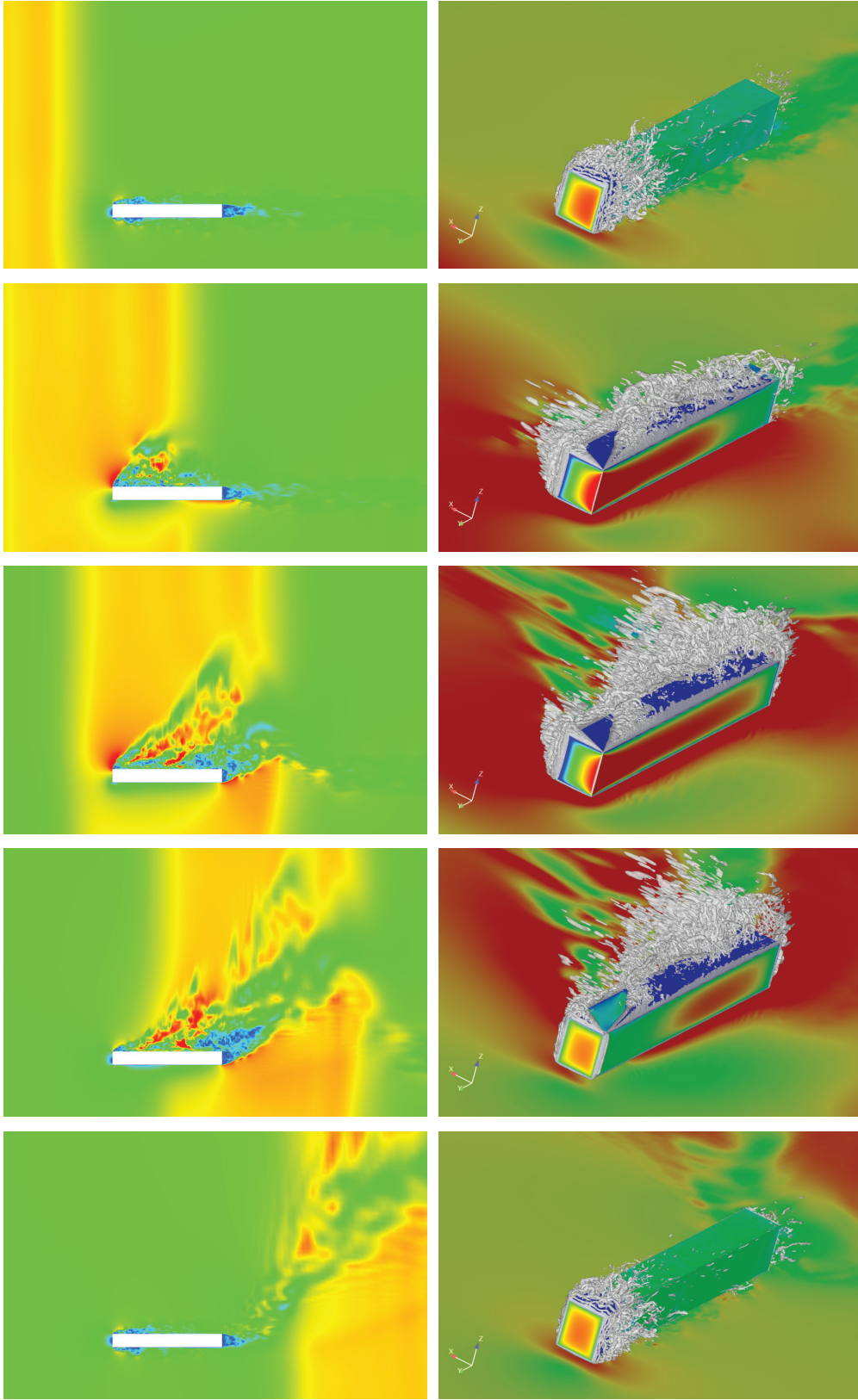


Figure 4.2.1: *LES flow. Left column: Instantaneous velocity field. Right column:  $Q$ -invariant =  $1e4$ , train body colored with pressure. Sample points at  $y = -540, -220, -30, 280$ , and  $680$  mm.*

#### 4.2.2 Validation with experimental pressure data

The pressure is here compared for the experimental measurement points 1-38. The LES and PANS data is plotted together with the experimental data for direct comparison. What can be observed in the comparison with experimental data is that LES and PANS is predicting the pressure in relatively similar manner. Many of the general transient pressure trends seem to be predicted, but the magnitude of the pressure is not always well predicted.

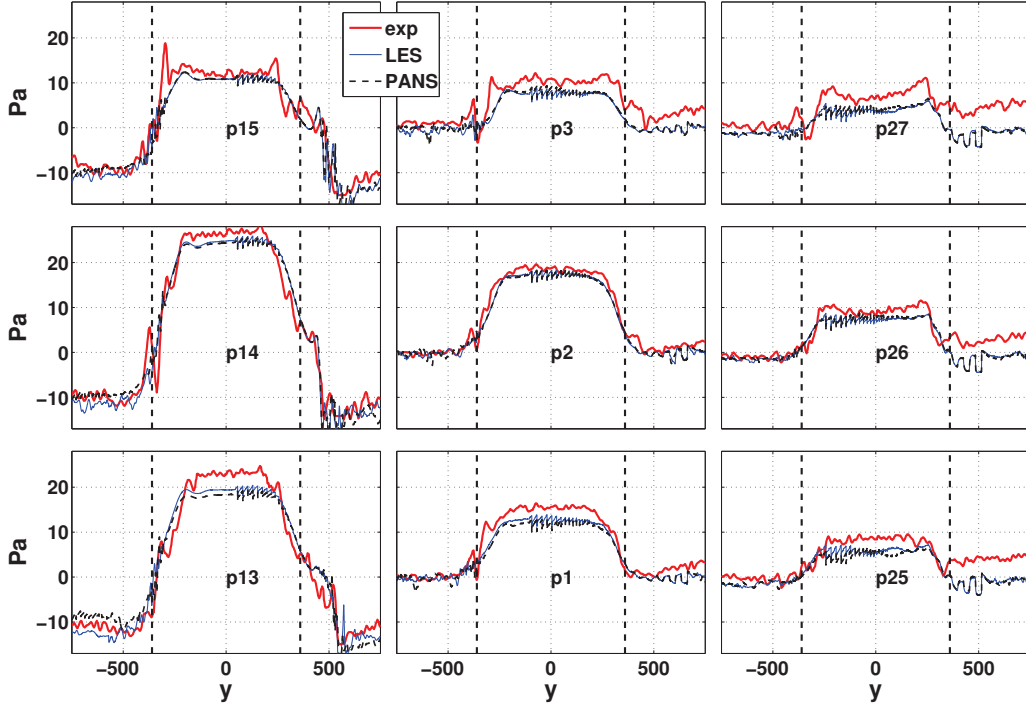


Figure 4.2.2: *Transient pressure graphs for the wind side points.*

Figure 4.2.2 contains all the transient pressure graphs for the measurement points situated on the wind side of the train body. The dashed vertical black lines marks the position of the wind tunnel nozzle. The pressure is generally underpredicted during the crosswind passage, indicating that the boundary layer on the wind side is not properly resolved. Figure 4.2.3 shows the pressure graphs on the lee side of the train body. The pressure in p. 19-21 indicate that the separation at the lee front of the train is hard to capture when the train is entering the crosswind region. This can be caused by inadequate resolution in the mesh, but lack of turbulence in the crosswind velocity profile might also contribute. Figure 4.2.4 shows that the pressure trends at the roof is harder to predict at the front of the train, in the vicinity of the quasi steady vortices (p. 17-18).



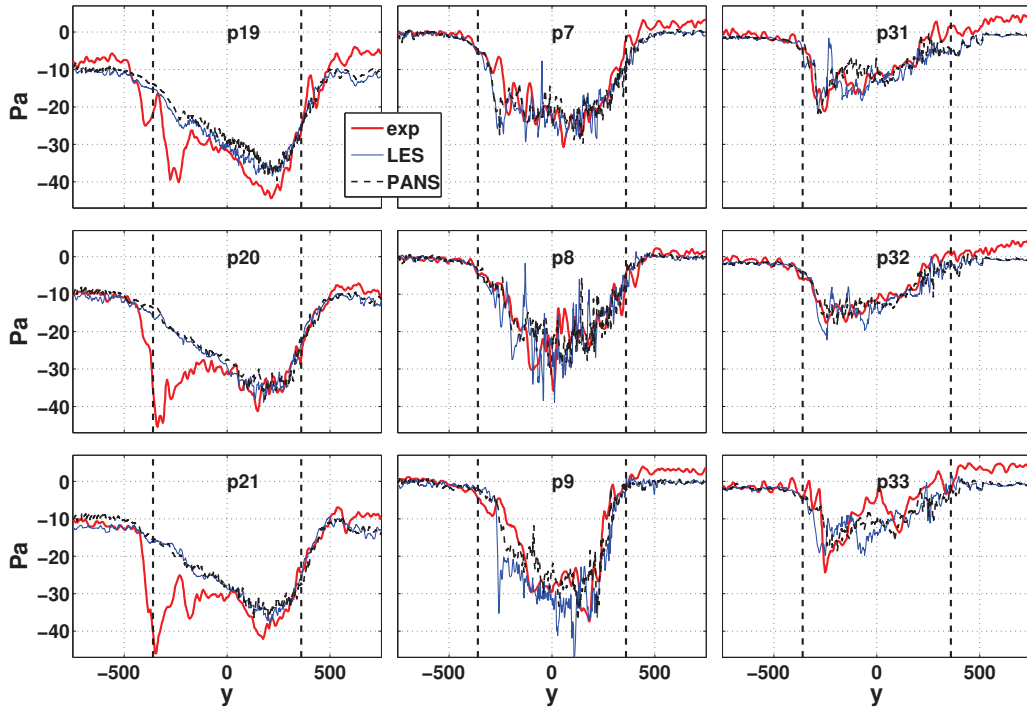


Figure 4.2.3: *Transient pressure graphs for the lee side points.*

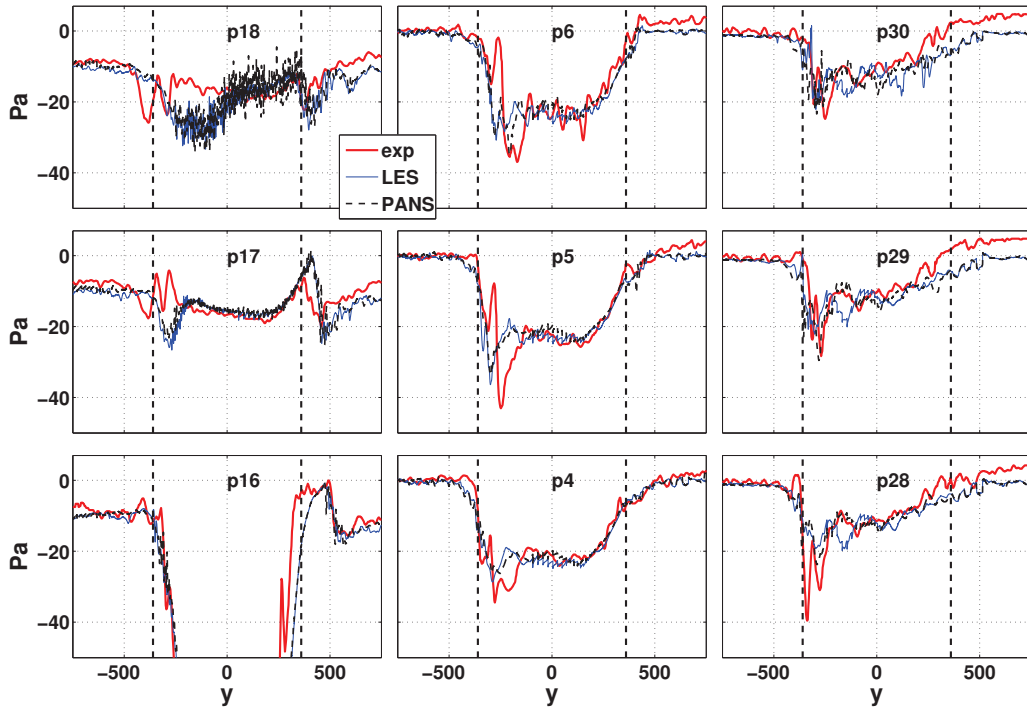


Figure 4.2.4: *Transient pressure graphs for the roof points.*

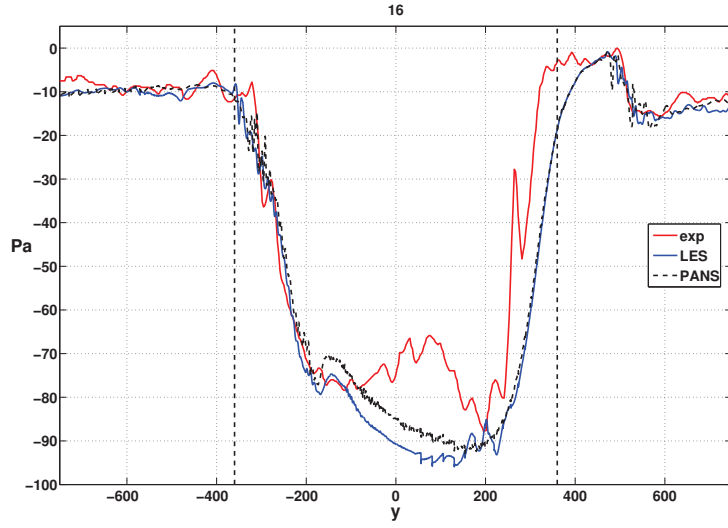


Figure 4.2.5: *Transient pressure at point 16.*

Figure 4.2.6 shows that the pressure magnitude is quite poorly predicted under the train at the front and midsection (p. 22-24 and 10-12). The symmetry condition on the ground slit under the train can't properly describe the cavity flow in the ground slit. On the other hand the distance between the ground and the train is quite large;  $H/3$  (where  $H$  is the train height). In the authors mind, the discrepancies is more likely to be caused by insufficient mesh resolution.

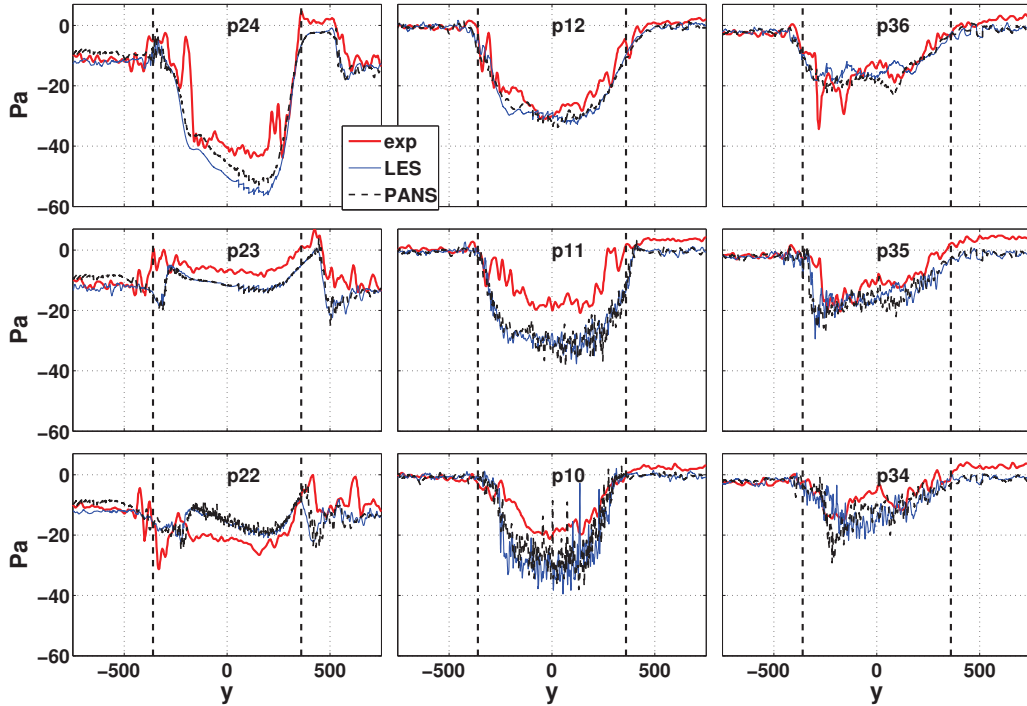


Figure 4.2.6: *Transient pressure graphs for the points under the train.*

Figure 4.2.7 shows the pressure on the front and rear of the train. The pressure oscillations seen at the front in the experimental data is not captured in the simulations. This indicates once again that the crosswind in the experiment contains oscillations that is not present in the smooth profile used in the simulation.

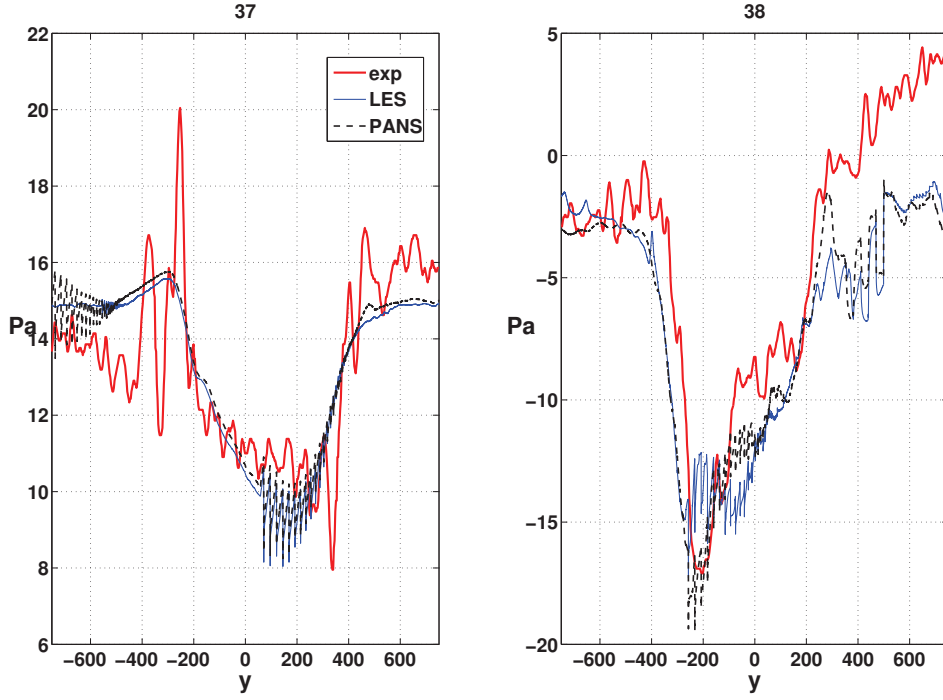


Figure 4.2.7: *Transient pressure graphs for the front (p. 37), and the rear (p. 38) face of the train.*

### 4.2.3 Force coefficients

To obtain the force coefficients, the maximum effective crosswind  $\sqrt{5^2 + 5^2}$  is used. To compare the stationary case with the moving, the unscaled forces are plotted. Note that the external crosswind is of the same magnitude in the moving and the stationary case, but the effective crosswind will be larger in the moving case. As expected the side force is greater when the train is moving than when stationary. This is displayed in figure 4.2.8.

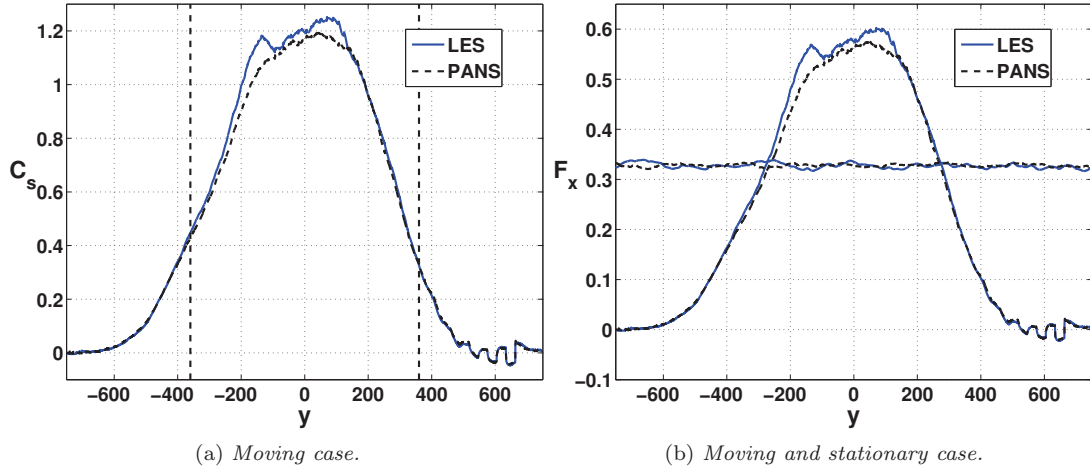


Figure 4.2.8: *Side force time history over the passage through the crosswind.*

The lift and drag force is also increased during the passage through the crosswind, as shown in figure 4.2.9 and 4.2.10. It can also be noted that LES and PANS shows some major differences in the side and lift force, which is not obvious when studying the pressure.

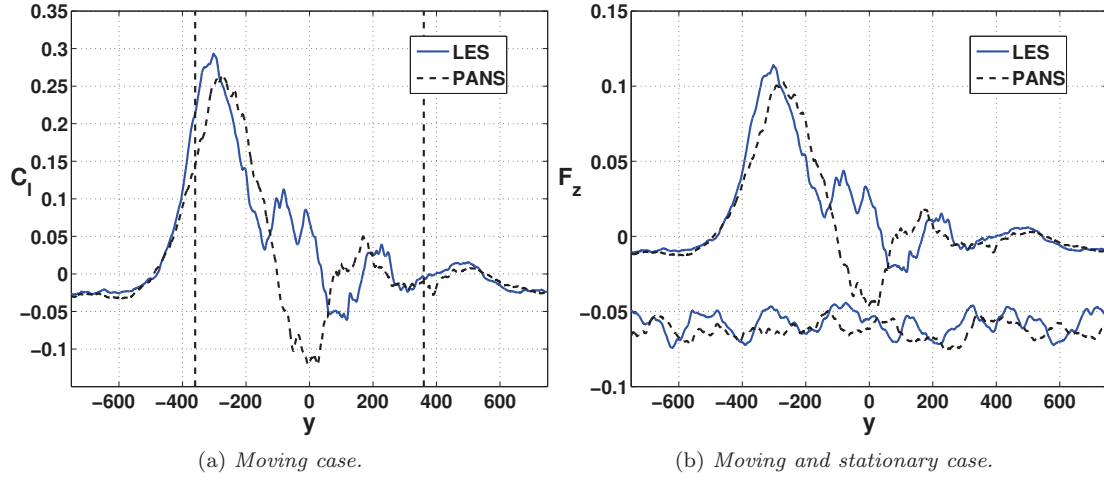


Figure 4.2.9: Lift force time history over the passage through the crosswind.

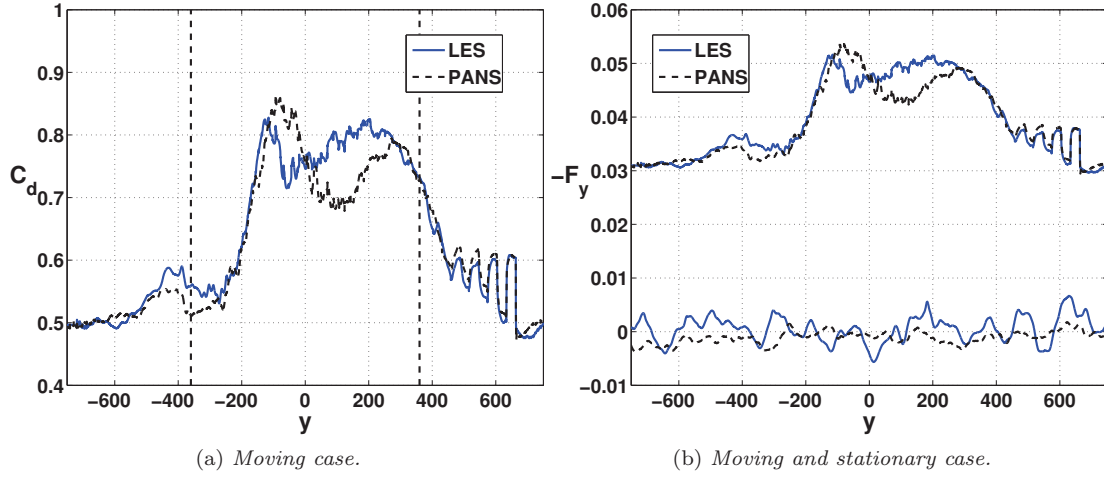


Figure 4.2.10: Drag force time history over the passage through the crosswind.

#### 4.2.4 Computation of $f_k$ for transient boundary conditions

As explained in section 2.3  $f_k$  is changing dynamically as  $f_k \sim \varepsilon_u^{2/3}/(k_u + k_r)$ . However,  $k_r$  is computed with the deviations from the averaged velocity. For the moving case, the velocity is constantly changing due to transient boundary conditions. This will cause the velocities to deviate strongly from the mean, which will incorrectly be computed as resolved TKE. Large values of  $k_r$  will give very low values of  $f_k$ , prohibiting a proper modelling of the unresolved turbulence. This scenario is shown in figure 4.2.11. The left column shows the velocity field from the same above view, in order to illustrate the train position relative the crosswind.

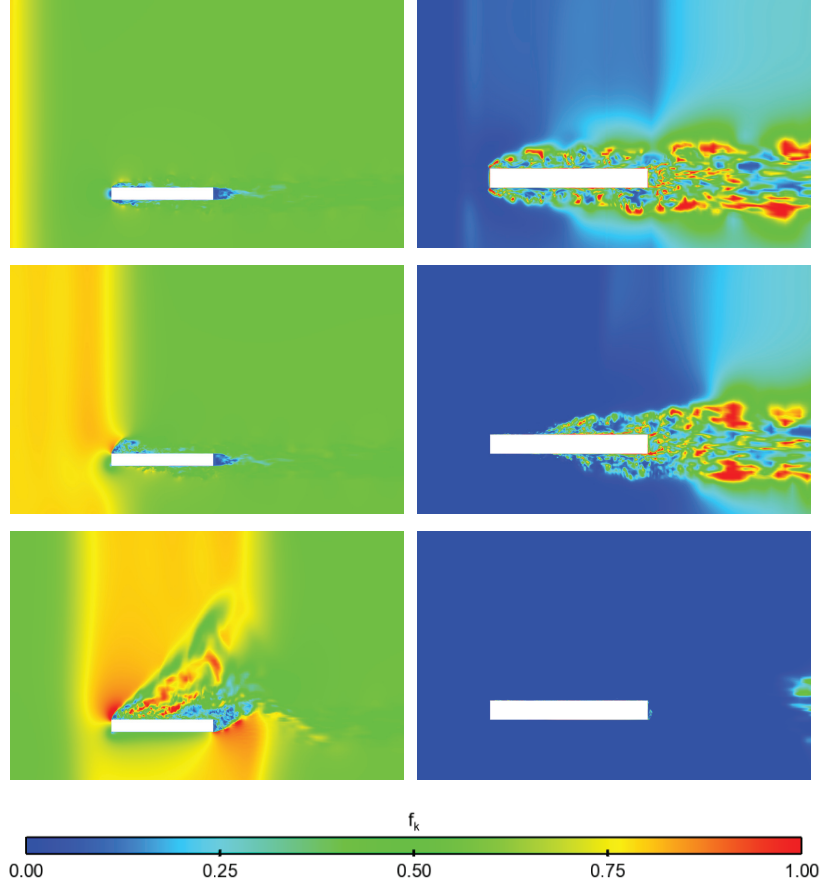


Figure 4.2.11: The parameter  $f_k$  at three different train positions:  $y = -720, 420$  and  $30$  mm. The right column shows velocity in the same  $z$ -plane to visualize the trains relative position to the side wind.

Figure 4.2.12 visualizes how the unresolved TKE  $k_u$  goes to zero as the the computed resolved TKE  $k_r$  increases. This shows clearly that computing  $f_k$  with the current definition of  $k_r$  is not suitable for the current flow scenario.

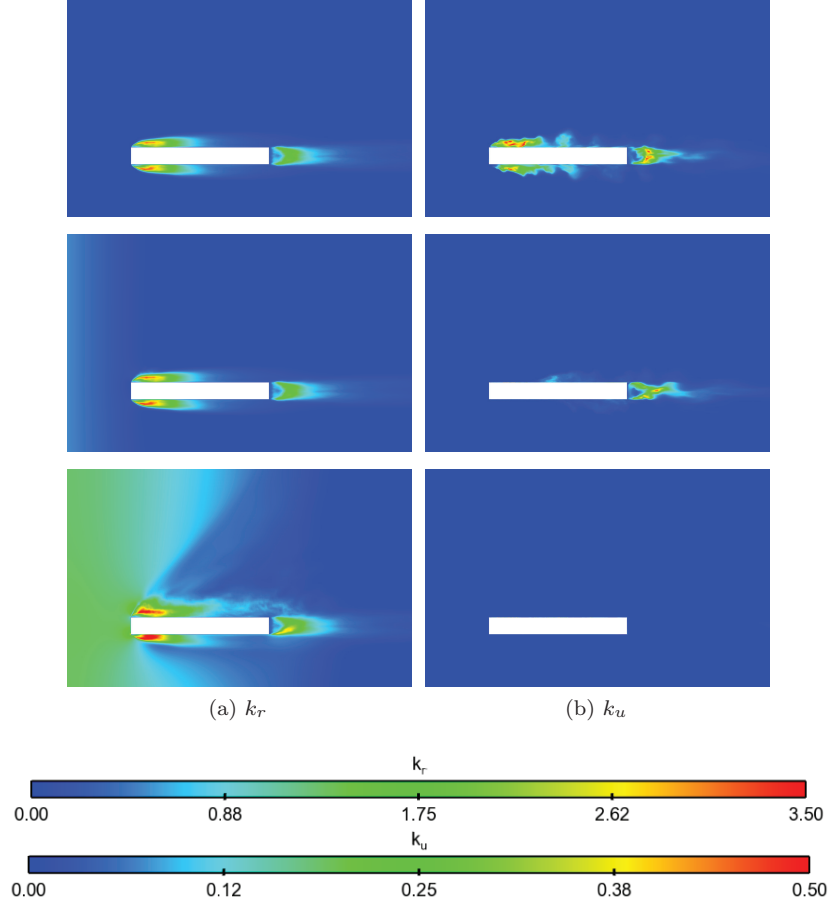


Figure 4.2.12: The resolved and unresolved TKE at three different train positions;  $y = -720, 420$  and  $30$  mm.

## 5 Discussion and Future Work

- PANS shows promising results for the stationary case. However, the geometry has sharp edges and therefore PANS ability to predict the separation point has not been tested. PANS  $\zeta$ - $f$  was tested on a finite cylinder in [2], and showed good results, but more investigations are needed.
- The resolution of the mesh is high enough to yield reasonable results with LES. The main target of the PANS method is to use an even coarser mesh, which still remains to be tested.
- For the moving case, the current way of calculating  $f_k$  is not suitable. For moving cases,  $f_k$  could be set to a constant, or perhaps  $k = k_u/f_k$  could be used to calculate  $f_k$ . Another suggestion is to solve the original URANS equation for  $k$  in parallel. For stationary cases, it would also be interesting to compare different ways to set  $f_k$ .
- For the moving case, the author believes that a moving crosswind boundary condition is sufficient to recreate the scenario. The first step is to refine the mesh. If the pressure predicted by LES still shows substantial discrepancies, imposed turbulence in the crosswind should be tested. This could be implemented as sinusoidal oscillations imposed on the smooth velocity profile. Prescribing the crosswind profile on the lee side is good because it ensures the propagation of the crosswind through the domain. However it could be interesting to try a pressure or neumann boundary condition instead.

# References

- [1] C. Baker. “The effect of unsteady crosswind forces on train dynamic behaviour.” In: *Proceedings of the 5th European and African Congress on Wind Engineering* (2009).
- [2] B. Basara, S. Krajnović, and S. Girimaji. “PANS Methodology Applied to Elliptic-Relaxation Based Eddy Viscosity Transport Model”. In: *Turbulence and Interactions*. Notes on Numerical Fluid Mechanics and Multidisciplinary Design 110 (2010). Ed. by M. Deville, T.-H. Lê, and P. Sagaut, pp. 63–69.
- [3] B. Basara, S. Krajnović, and S. Girimaji. “PANS vs LES for computations of the flow around a 3D bluff body”. In: *Engineering Turbulence Modelling and Measurements*. 7th International ERCOFTAC Symposium (2008).
- [4] L. Davidson. *Fluid mechanics, turbulent flow and turbulence modeling*. Chalmers, 2011, pp. 140–160. URL: [http://www.tfd.chalmers.se/~lada/postscript\\_files/solids-and-fluids\\_turbulent-flow\\_turbulence-modelling.pdf](http://www.tfd.chalmers.se/~lada/postscript_files/solids-and-fluids_turbulent-flow_turbulence-modelling.pdf).
- [5] S. Girimaji. “Partially-Averaged Navier-Stokes model for turbulence: Implementation and Validation”. In: *43rd AIAA Aerospace Sciences Meeting and Exhibit*. Notes on Numerical Fluid Mechanics and Multidisciplinary Design 10-13 January, Reno, Nevada (2005).
- [6] K. Hanjalic, M. Popovac, and M. Hadziabdic. “A robust near-wall elliptic-relaxation eddy-viscosity turbulence model for CFD”. In: *International Journal of Heat and Fluid Flow* 25.6 (2004), pp. 1047–1051. URL: <http://www.sciencedirect.com/science/article/pii/S0142727X0400116X>.
- [7] H. Hemida and S. Krajnović. “Exploring Flow Structures Around a Simplified ICE2 Train Subjected to a 30 Degree Side Wind Using LES.” In: *Journal of Engineering Applications of Computational Fluid Dynamics* 3(1) (2009), pp. 28–41.
- [8] S. Krajnović and L. Davidson. “Large Eddy Simulation of the Flow Around an Ahmed Body.” In: *Proceedings of the ASME Heat Transfer*. Fluids Engineering Summer Conference 2004 (2004), pp. 653–662.
- [9] S. Krajnović and L. Davidson. “Large Eddy Simulation of the Flow Around an Ahmed Body.” In: *SAE Paper 2004-01-0227* (2004).
- [10] S. Krajnović, J. Georgii, and H. Hemida. “DES of the Flow Around a High Speed Train under the Influence of Wind Gusts.” In: *Engineering Turbulence Modelling and Measurements*. 7th International ERCOFTAC Symposium (2008).
- [11] J. Smagorinsky. “General Circulation Experiments with the Primitive Equations.” In: *Monthly Weather Review* 91(3) (1963), pp. 99–165.
- [12] H. K. Versteeg and V. W. *An Introduction to Computational Fluid Dynamics*. Second Edition. Person Education Limited, 2007, p. 43.